Quaternary Science Reviews 328 (2024) 108525

Contents lists available at ScienceDirect

Quaternary Science Reviews

journal homepage: www.elsevier.com/locate/quascirev

Nondestructive geochemical characterization of fossil hominin taphonomy and burial history

Theodore M. Present [a,*], Elizabeth M. Niespolo [a,1], Catherine E. Clarke [b], Anna K. Behrensmeyer [c], Louise N. Leakey [d,e], Meave G. Leakey [d,e], Carrie Mongle [d,e], Anton Du Plessis [f], Paul Northrup [g], Ryan V. Tappero [h], Deming Yang [e,2], E. Troy Rasbury [g], Fredrick E. Grine [d,i]

[a] Division of Geological and Planetary Sciences, Caltech, 1200 E. California Blvd., m/c 100-23, Pasadena, CA, 91125, USA
[b] Department of Soil Science, Stellenbosch University, Stellenbosch, South Africa
[c] Department of Paleobiology and Human Origins Program, National Museum of Natural History, Smithsonian Institution, Washington, DC, 20013, USA
[d] Department of Anthropology, Stony Brook University, Stony Brook, NY, 11794, USA
[e] Turkana Basin Institute, P.O. Box 24467, 00502, Nairobi, Kenya
[f] CT Scanner Facility, Stellenbosch University, Stellenbosch, South Africa
[g] Department of Geosciences, Stony Brook University, Stony Brook, NY, 11794, USA
[h] NSLS-II, Brookhaven National Laboratory, Upton, NY, 11973, USA
[i] Department of Anatomical Sciences, Stony Brook University, Stony Brook, NY, 11794, USA

ARTICLE INFO

Handling editor: Mira Matthews

Keywords:
Pleistocene hominin
Koobi Fora Formation
Turkana Basin
Geochemical taphonomy
Fossilization
X-ray microanalysis
Fossil diagenesis

ABSTRACT

To date, only three *Homo habilis* specimens have been discovered that have associated craniodental and postcranial elements, providing a limited fossil record of the ontogeny and morphology of early members of the genus *Homo*. Recently, a nearly complete dentition, likely attributable to *H. habilis*, was discovered and excavated from early Pleistocene-age fluvial-lacustrine sediments of the upper Burgi Member of the Koobi Fora Formation at site F25787 in Area 13, near Ileret, Kenya. On the surface less than 15 m away, at site F25966, postcranial elements were found, which, if from the same individual as the nearby dentition, would represent the fourth associated craniodental and postcranial assemblage of this species. We developed a geochemical taphonomic history of these *ca.* 2 Ma hominin fossils using nondestructive X-ray based microanalytical tools (synchrotron and benchtop X-ray fluorescence chemical imaging and micro- and nano-computed tomography volumetric reconstruction), bulk analyses of sediments and paleosols at the excavation sites, and sedimentologic and stratigraphic observations. We integrate the chemical and physical taphonomic histories to test whether teeth (excavated *in situ*) and postcranial bones (eroded onto the outcrop surface) derive from a single individual. Minor differences in taphonomic history are attributable to the different biomineral properties of the dental and osseous components and to differences in physical damage during early post-mortem scavenging, dispersal, and burial in adjacent depositional settings. Microscale geochemical mapping enabled the temporal ordination of chemical and physical events in the specimens' chemical taphonomic histories. Specifically, authigenic Fe- and K-bearing clays and Y, U, and Sr uptake occurred in post-burial fractures in bones and were also incorporated pervasively throughout dentin in teeth. Barite mineralization occurred along the latest fractures in both materials, and as a coating on tooth roots. The stratigraphic, taphonomic, and geochemical evidence supports the interpretation that the

Abbreviations: CRM, certified reference materials; CT, computed tomography; EDS, energy dispersive spectroscopy; HAp, hydroxyapatite; LC, left canine; LM, left molar; LOI, loss on ignition; LP, left premolar; RC, right canine; RM, right molar; ROI, region of interest; RP, right premolar; XANES, X-ray absorption near edge structure; XAS, X-ray absorption spectroscopy; XRF, X-ray fluorescence.

* Corresponding author. Division of Geological and Planetary Sciences, Caltech, 1200 E. California Blvd., m/c 100-23, Pasadena, CA, 91125, USA.
E-mail addresses: ted@caltech.edu (T.M. Present), niespolo@princeton.edu (E.M. Niespolo), cdowding@sun.ac.za (C.E. Clarke), behrensa@si.edu (A.K. Behrensmeyer), louise.leakey@stonybrook.edu (L.N. Leakey), meave.leakey@stonybrook.edu (M.G. Leakey), carrie.mongle@stonybrook.edu (C. Mongle), anton2@sun.ac.za (A. Du Plessis), paul.northrup@stonybrook.edu (P. Northrup), rtappero@bnl.gov (R.V. Tappero), dyang@amnh.org (D. Yang), troy.rasbury@stonybrook.edu (E.T. Rasbury), frederick.grine@stonybrook.edu (F.E. Grine).
[1] Present address: Princeton University, 218 Guyot Hall, Princeton, NJ, 08544, USA.
[2] Present address: Division of Anthropology, American Museums of Natural History, 79th Street at Central Park West, New York, NY, 10024, USA.

https://doi.org/10.1016/j.quascirev.2024.108525
Received 28 September 2023; Received in revised form 26 January 2024; Accepted 28 January 2024
Available online 15 February 2024

hominin fossils represent a single individual. Successful application of these nondestructive sample characterization methods demonstrates capabilities for thorough interrogation of the taphonomic histories of other potential hominin fossil associations, enabling more robust and accurate palaeontologic constraints using those relationships.

1. Introduction

Hominin fossils are the precious evidence for human evolution collected from the geologic record. Some fossils, such as teeth, provide ontogenetic constraints on the individual's development and age prior to its death. Others, especially skull fragments and postcranial bones, yield morphologic characteristics such as the individual's size and sex. When various skeletal components that comprise associated assemblages derive from single individuals, they provide unusually important contributions to the hominin evolutionary record. However, most hominin fossils are found scattered on outcrop surfaces and occur in a wide range of depositional settings. Such fragmentary fossil remains of individual hominins are informative but their incompleteness limits interpretations of hominin anatomy and evolution (Grine et al., 2022).

Fragmentary but spatially associated hominin fossils were discovered in lower Pleistocene (>1.87 Ma) strata exposed and excavated in the upper Burgi Member of the Koobi Fora Formation in Area 13, Ileret, Kenya. These consist of a nearly complete lower dentition of an adult individual (specimen KNM-ER 64060, discovered in 2012 at locality F25787) and postcranial bones representing multiple upper limb elements from both sides of an adult hominin skeleton (specimen KNM-ER 64061, also discovered nearby in 2012 but given a separate locality number F25966). These closely related fossil localities will be referred to collectively as F25787–F25966. The dentition has been attributed to an early member of the genus *Homo*, with its strongest resemblances to other dentitions that have been referred to *H. habilis* (Grine et al., 2019). The postcranial bones are hypothesized to derive from the same individual based on their recovery in very close proximity (within 15 m) to the dentition and the absence of any skeletal element duplication. In this case and others, independent testing of the proposed association between teeth and postcranial bones is important, especially because such associations are uncommon in the hominin record.

Fossil vertebrate remains typically may have experienced numerous pre-and post-burial taphonomic processes, including scavenging, transport, chemical and physical weathering, and bioturbation followed by post-burial diagenesis and exhumation (Behrensmeyer, 1978; Hedges, 2002; Kendall et al., 2018; Trueman, 2013; Turner-Walker, 2008). Disentangling the later stages of this history is particularly challenging when destructive analyses are untenable, as diagenesis frequently affects the primary geochemistry and texture of bone biominerals (Hedges, 2002; Kendall et al., 2018; Kohn et al., 1999; Lambert et al., 1985; Parker and Toots, 1970; Tütken et al., 2008). Nondestructive analytical techniques may help to overcome many of these challenges. Synchrotron X-ray absorption spectroscopy (XAS) and X-Ray Fluorescence (XRF) mapping, nano- and micro-Computed Tomography (CT), and benchtop μXRF are nondestructive techniques suited for determining mineralogy and mapping element abundances in fossil bones and teeth. Sediment chemistry determined by XRF analyses and soil chemical extraction techniques applied to disaggregated sedimentary rocks and paleosols provide geochemical context for the modern and ancient sediments and the groundwater fluids that may have interacted with and altered the fossils (Morley et al., 2023; Retallack, 1988).

Comparing the geochemical histories of teeth and postcranial bones is also challenging due to how different primary biomineral compositions behave during diagenesis (Parker and Toots, 1980; Turner-Walker, 2008). Dentin and enamel in teeth, mandibular and maxillary bone closely associated with teeth, and bone comprising postcranial elements, are all composed of the biomineral hydroxyapatite (HAp, $Ca_{10}(PO4)_6(OH)_2$) but differ in primary porosity, organic content, and water content (Cacciotti, 2016; Driessens and Verbeeck, 1990; Turner-Walker, 2008). These various primary biomaterials react differently to environmental and diagenetic conditions, but studies of how diagenesis affects the composition of mammalian (including hominin) biominerals depend on local conditions and are often destructive to the fossil samples (e.g., France et al., 2020; Kendall et al., 2018; Kohn et al., 1999; Lambert et al., 1985; Schoeninger et al., 2003; Tütken et al., 2008; Wang and Cerling, 1994). Thus, we also include in our nondestructive analyses a single fossil mammal jaw fragment that includes a tooth with both dentin and enamel still attached to bone. This jaw fragment derives from a different stratigraphic level (the KBS Member of the Koobi Fora Formation, which overlies the Burgi Member) and a different locality in Area 13 of the Ileret region (locality F26222), but it includes all three primary biominerals found among the associated F25787–F25966 dentition and postcranial bone fossils. Because all three biominerals occur in a single fragment, we use it to control for the effects of primary biomineral variability on geochemical alteration of samples that experienced a shared diagenetic history.

Using nondestructive geochemical analyses, we develop and compare chemical taphonomic histories for the teeth and postcranial fossils at F25787–F25966. By comparison to the geochemical heterogeneity of the F26222 fossil control from the KBS Member, we assess which geochemical variations among the upper Burgi Member fossils at F25787–F25966 can be attributed to differences in primary biomineral composition and/or to diagenetic processes affecting the bones and teeth.

2. Geologic setting of the hominin fossils

Pliocene to Holocene strata in the Omo-Turkana Basin that outcrop around Lake Turkana (Kenya and Ethiopia) are lacustrine, alluvial, and volcanic rocks containing a rich early hominin fossil record (Behrensmeyer, 1970; Isaac et al., 1971; Leakey and Leakey, 1978; Leakey, 1970). After the discovery on the surface of four isolated hominin mandibular teeth, excavation at the site recovered additional teeth comprising a nearly complete set attributed to a young adult *H. habilis* from the upper Burgi Member of the Pleistocene Koobi Fora Formation along Kolom Odiet (Area 13, Brown and Feibel, 1986), at locality F25787 (4° 15.682′ N, 36° 20.044′ E) near Ileret, Kenya (Fig. 1, Fig. 2A and B). Very close to this site, numerous postcranial bones (Fig. 2C and D) were found in a limited area on the outcrop surface, within 12–15 m of the dentition site (Fig. 3B; Grine et al., 2019); these were given a separate designation as F25966 (4° 15.675′ N, 36° 20.041' E). Although the postcranial remains are clearly associated on the outcrop surface and in good condition, indicating recent emergence from the enclosing deposits, further excavation did not document any additional hominin remains *in situ*.

The Burgi Member consists of 55 m of siltstones and sandstones that overly the Tula Bor Member on an angular unconformity (Fig. 1A, Gathogo and Brown, 2006). Using Area 13 stratigraphic observations made by F. H. Brown (unpublished, 2014), samples were correlated to Section PNG-10.1 (Fig. 1B), a stratigraphic section of the upper Burgi Member described in Gathogo and Brown (2006). At F25787–F25966, over multiple years (2012–2018) of research at these localities, seven trenches were excavated through several sedimentary units exposed in northwest-dipping strata about 40 m below the KBS Tuff. This tuff, dated at *ca.* 1.87 Ma, marks the base of the KBS Member of the Koobi Fora Formation (Grine et al., 2019; Joordens et al., 2013; McDougall and Brown, 2006). The teeth derived from a 1–2 m thick yellow-gray (7.5 YR

6/1) clayey siltstone (Fig. 1C), which lacks primary sedimentary layering but contains pedogenic structures including root traces, calcite concretions, manganese oxide and limonite nodules, and blocky fractures with later selenite deposits. The clayey siltstone is overlain by a sandy siltstone followed by interbedded clayey and sandy silts, capped by a fine-grained, tabular sandstone bearing lacustrine fossils such as fish bones, ostracods, bivalves, and *Bellamya* gastropods (Fig. 1C).

Four hominin teeth were found on the surface of the outcrop (Fig. 3),

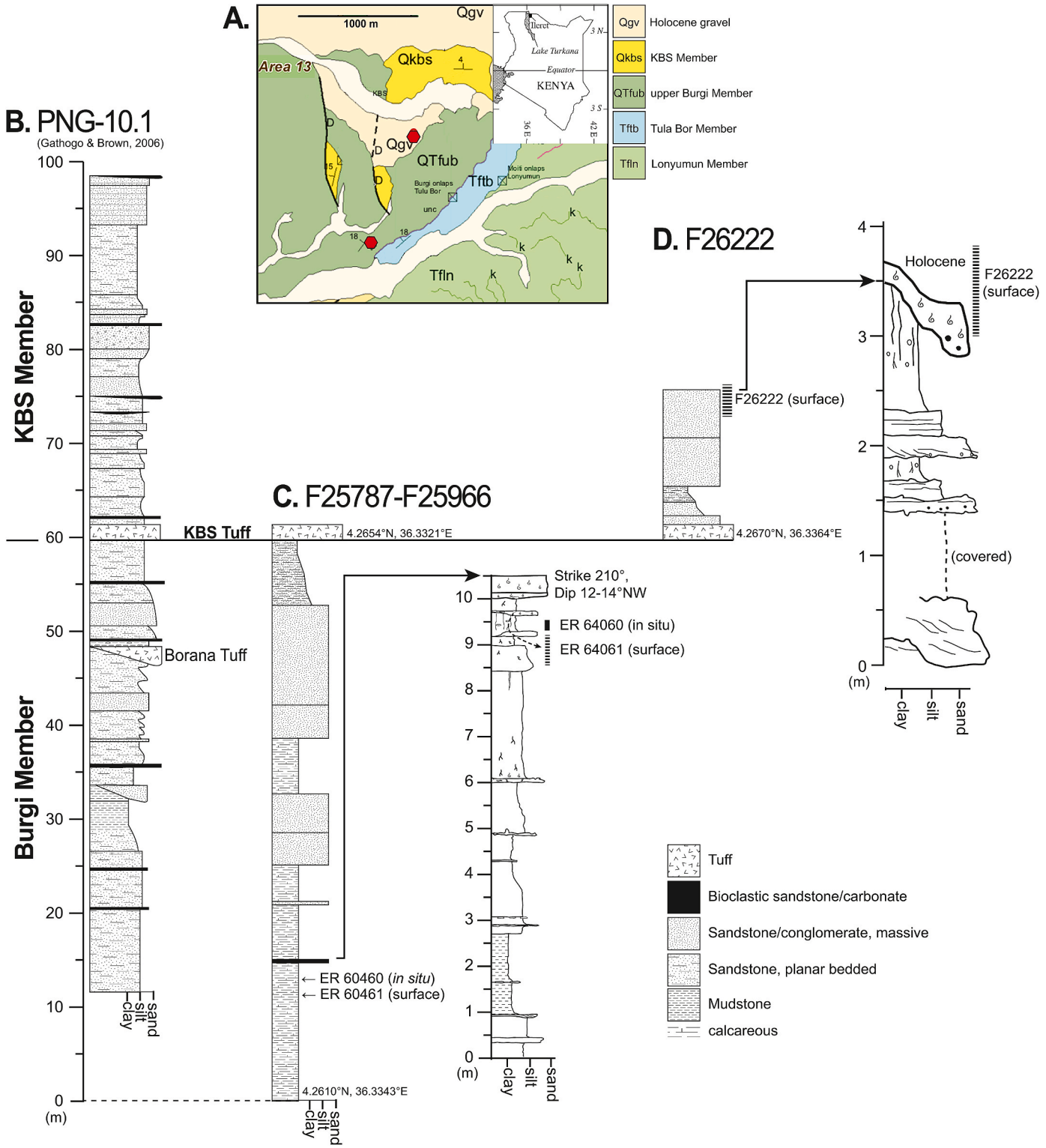

Fig. 1. (A) Geologic map of the upper Koobi Fora Formation at Area 13 near Ileret, Kenya (inset) showing hominin sites F25787–F25966 and F26222 (red octagons), (Connors and Raynolds, 2022). (B) Koobi Fora Formation stratigraphic section PNG-10.1 (adapted from Gathogo and Brown, 2006) in Area 13 near Ileret, Kenya. (C-D) Measured sections through fossil localities by F. H. Brown (unpublished, 2014) correlated with detailed sections by AKB showing stratigraphic positions of KNM-ER 64060 teeth (*in situ*) KNM-ER 64061 postcranial elements (surface) at F25787–F25966 (C) and surficial hominin and mammalian fossils at F26222 (D). Dashed vertical bars show estimated stratigraphic range of surface finds, solid bar for *in situ* fossils.

and when the underlying sediment was excavated, eleven additional teeth, many with complete roots, were found *in situ* within a limited area (40 × 40 cm) and distributed vertically through 43 cm of the clayey siltstone. These form a nearly complete lower dentition (Fig. 2A), clearly from a single individual, lacking all evidence of the mandibular corpus except for minor remnants of mandibular alveolar bone between tooth roots (Fig. 2B). The teeth were together assigned a Kenyan National Museum accession number KNM-ER 64060 (Fig. 2A and B). Multiple fragmentary postcranial bones (F25966) were discovered on the eroded exposure of the dipping sediments, 10–25 m (predominately clustered near 12 m) laterally and downslope from the top of the tooth-bearing unit (Fig. 3B). Fossil bones and teeth of other mammals were also discovered in this same area.

The hominin teeth and postcranial bones are derived from spatially and sedimentologically closely related strata, and therefore plausibly from the same individual. The lack of duplicated fossil fragments and ontogenetic indicators that both sets of fossils are adult support this possibility. However, because of the spatial displacement of the postcranial bones from the *in situ* teeth, and the fact that the source of the teeth was confirmed by excavation while the source of the postcranial bones was not, the latter were originally assigned a separate locality number, F25966, and later a separate accession number, KNM-ER 64061 (Fig. 2C).

Mammalian faunal mandibular and postcranial bone fragments were also discovered in the overlying KBS Member of the Koobi Fora Formation, 870 m north-northeast of F25787–F25966, at a locality called F26222 (Fig. 1A and D, 4° 16.1′ N, 36° 20.21’ E). These are derived from a younger sedimentary unit with a different depositional and diagenetic history but retain the same suite of primary biomaterials discovered at F25787–F25966 (i.e., fossilized tooth dentin, mandibular bone, and postcranial bone). The F26222 non-hominin mammal remains were used as a control for variation in different biomaterials from the same site and also for comparison with the diagenetic geochemistry of F25787–F25966.

3. Methods

3.1. Excavation and sedimentary analysis

Following excavation of the KNMER-64060 teeth and discovery of the surficial bones at F25787–F25966, an additional trench (Trench 7, Supplemental Fig. 1) was excavated in 2017 parallel to strike, situated at the base of the outcropping *Bellamya*-bearing sandstone bed that overlies the tooth-bearing clayey siltstone. This excavation was intended to search for additional *in situ* fossils, characterize the detailed vertical stratigraphy and sedimentology at the tooth discovery site, and examine lateral (along-strike) sedimentologic variability between the *in situ* teeth and surficial bone discovery sites.

After excavation, ten sedimentary rock samples were collected from F25787–F25966 in 2018 by Cyprian Nyete for geochemical analysis (Table 1, Fig. 3, Supplemental Dataset 1, Supplemental Fig. 1). Samples were collected at the location of the dentition and at the approximate level of the postcranial surface specimens (samples 2 and 4, respectively), as well as from surrounding sediments above, below, and laterally east and west from the fossil locations. Samples were lightly crushed using a mortar and pestle and passed through a 2 mm sieve; there were few to no fragments coarser than 2 mm.

3.1.1. Particle size analysis

Particle size analysis was conducted on disaggregated sandstone and siltstone samples following the pipette method of Gee and Bauder (1986). Prior to dispersion, organic matter and carbonates were removed using 30 % H_2O_2 and 1 M sodium acetate adjusted to pH 5 with acetic acid, respectively. Samples were dispersed using 5 % Calgon solution (Na_2CO_3+ $(NaPO_4)_6$). Dispersed sediment samples were passed through five sieves (mesh sizes: 1.00, 0.50, 0.250, 0.106 and 0.053 mm) and the fractions determined gravimetrically after drying. The remaining silt and clay size fractions of the dispersed sediment were determined using settling times and pipette extraction from a 1 L sedimentation tube.

3.1.2. Major and trace element analysis

Rock samples were milled to <70 μm. Major and trace element analyses were conducted on glass disks and compressed pellets, respectively. Glass disks were prepared for XRF analysis using 7 g of high purity trace element and rare earth element-free flux ($LiBO_2$ = 32.83 %, $Li_2B_4O_7$ = 66.67 %, LiI = 0.50 %) mixed with 0.7 g of the powdered sample. Mixtures of sample and flux were fused in platinum crucibles with a Claisse M4 gas fluxer at temperatures between 1100°C and 1200 °C. Pressed powder pellets were prepared for XRF analysis using 8 g of

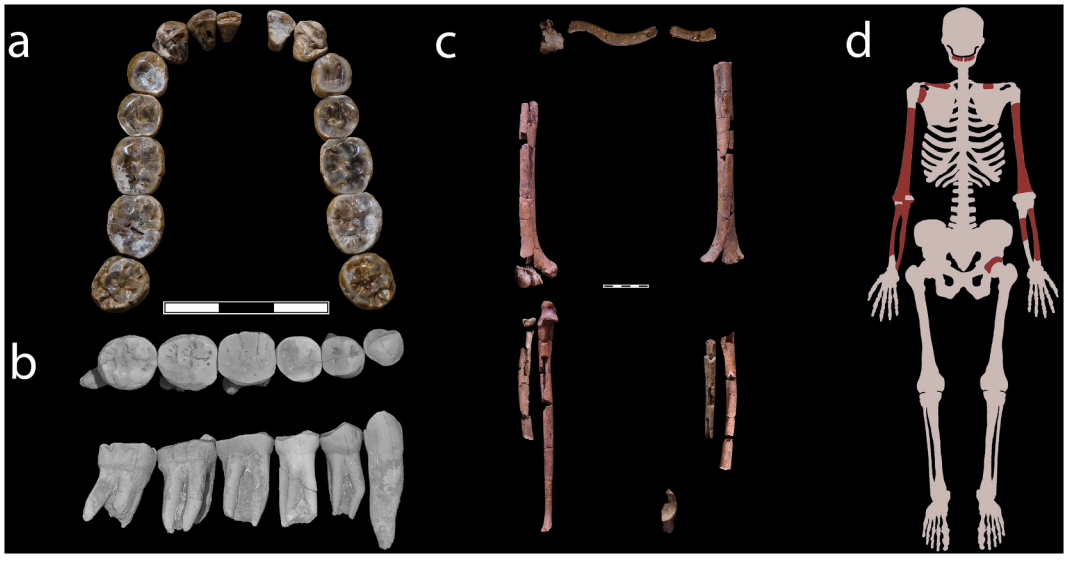

Fig. 2. Hominin fossils from the F25787–F25966 locality. (a) Occlusal view photographs of the KNM-ER 64060 dentition in anatomical alignment reproduced from Grine et al. (2019), scale in centimeters. (b) Occlusal and lateral views of the anatomical arrangement of RC-RM_3 of KNM-ER 64060 reconstructed from volumetric renderings of nano-CT scans of the individual tooth reproduced from Grine et al. (2019). Note remnant, deteriorated mandibular alveolar bone between tooth roots. (c) Anatomical arrangement of postcranial bone fragments of KNM-ER 64061, scale in centimeters. (d) Positions of fossils on a hominin skeleton.

the rock sample and a few drops of MOVIOL for bonding. Loss on ignition (LOI) was calculated by determining the weight change after igniting the samples at 1000 °C in a muffle furnace.

Elemental compositions were determined by XRF spectrometry on a PANalytical Axios Wavelength Dispersive spectrometer at the Central of Analytical Facilities, Stellenbosch University, South Africa. The certified reference materials (CRM) that were used in the calibration procedures for major and trace element analyses fit the range of concentrations of the samples, with the exception of high Cl in sample 10. Four sediment CRMs (S-20, S-14, S-19) and one marine mud CRM (MAG-1) were included in the calibration. Additional CRM's were selected as control standards and include NIM-G (Granite from the Council for Mineral Technology, South Africa) and BE-N (Basalt from the International Working Group). An in-house quality control standard (HUGS-1) was

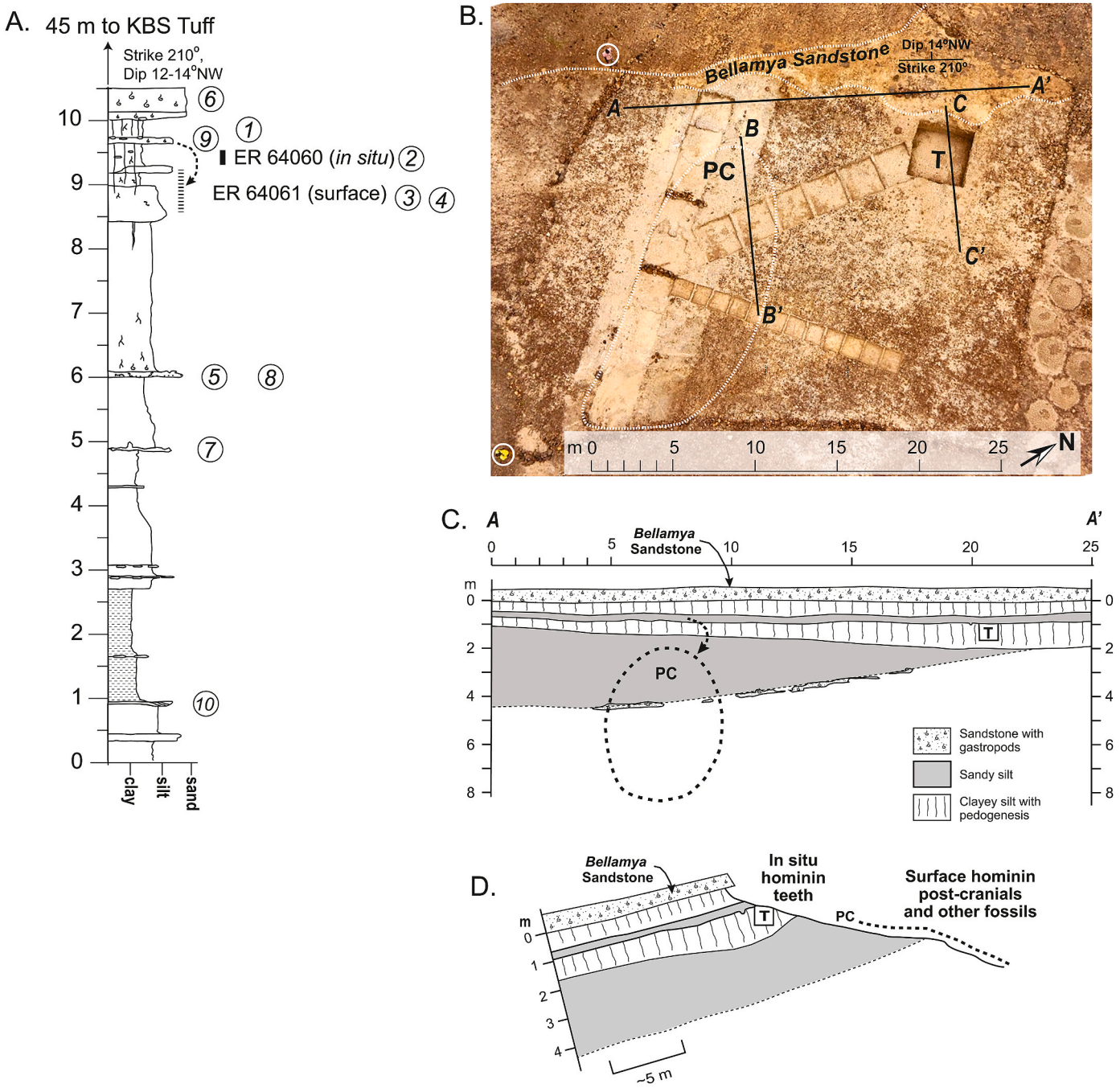

Fig. 3. Stratigraphic column and sedimentologic cross-sections of the F25787–F25966 locality. (A) Vertical stratigraphy by AKB showing the succession of lake margin lithofacies and the source units for sediment samples (circled numbers), with the curved dotted arrow indicating how postcranial fossils were interpreted to have eroded from overlying fossiliferous sandy siltstone. (B) Aerial (kite) photograph taken in 2014 of the excavations at F25787–F25966, showing the positions of KNM-ER 64060 (teeth found *in situ* at location 'T'), and surface scatter of postcranial elements KNM-ER 64061 (dotted area labelled PC) about 12 m along depositional strike from the teeth. Line A-A′ follows structural strike (210°) of sandstone bed (14° dip to the NW) that overlies the units with vertebrate fossils. Rock barrier shows the area of surface screening (Supplemental Table 1). Note circled people for scale. (C) Cross-section of sedimentologic variability approximately along strike (line A-A′ in B), showing relationship of the surface postcranials (PC) and the *in situ* tooth site (T). Dotted area shows the highest elevation and down-slope distribution of surface postcranial bones. (D) Cross section of inferred subsurface dip-transect sedimentary units; the highest (surface) postcranial element (PC = distal humerus) was (stratigraphically) < 1.0 m below lowest *in situ* hominin tooth. D represents a composite of lines B–B′ and C–C′ in B.

Table 1
Disaggregated sedimentary rock location, descriptions, and compositions at locality F25787–F25966.

No.	Location description	Sand (%)	Silt (%)	Clay (%)	Texture
1	Trench wall above dentition level (below *Bellamya* sandstone)	27.9	70.4	1.6	sandy siltstone
2	Trench wall at KNM-ER 64060 dentition excavation level	7.2	80.1	12.7	clayey siltstone
3	Level between teeth (F25787) and postcrania (F25966), outside of Trench 3	21.9	65.5	12.6	sandy siltstone
4	Trench wall at highest level of postcranial bone KNM-ER 64061 surface discovery	7.1	82.9	10.0	siltstone
5	Below postcrania level close to stone erosion barrier	33.6	52.9	13.5	sandy siltstone
6	Outcropping *Bellamya* sandstone 35 m southwest of postcrania	60.1	24.9	15.0	clayey, silty sandstone
7	15 m south-southeast of postcrania below postcrania level	5.7	84.7	2.4	sandy siltstone
8	Below dentition level 20 m southeast of teeth excavation	14.2	73.3	12.4	sandy siltstone
9	Possible postcrania source bed, outcropping southwest of post-crania discovery site	41.2	43.8	15.0	sandy siltstone
10	30 cm below surface in bank of a shallow modern channel 50 m southeast of teeth excavation	9.7	86.0	4.3	siltstone

also prepared as a glass disk and analyzed along with the samples. Accuracy of XRF measurements, provided in Dataset 1, are better than 10 % for all major elements and most trace elements.

3.1.3. Clay fraction mineralogy

Clay fractions were collected through dispersion and sedimentation after prior removal of organic matter and carbonates (as described in section 3.1.1). Dispersed clay samples were split into two and flocculated using either 1 M KCl or 0.5 M $MgCl_2$. Flocculated samples were washed through sequential washes with deionized water and increasing proportions of ethanol until the suspensions tested negative for Cl^- by adding a few drops of 0.1 M $AgNO_3$. Magnesium and K saturated clays were dried and gently crushed into a powder. X-ray diffraction analysis was conducted at iThemba labs on the randomly orientated clay extract powders with a step-size of 0.05° and a step-time of 40 s using a Bruker D8 Advance Powder Diffractometer with a graphite monochromator, using a Cu-Kα source at 40 mA and 40 kV.

3.2. Fossil analyses

3.2.1. Micro- and nano-CT

Fossil specimens (KNM-ER 64060, 64061) were scanned using non-destructive X-ray computed tomography at the Stellenbosch University CT Scanner Facility (Du Plessis et al., 2016). Teeth comprising the KNM-ER 64060 dentition were individually scanned using a General Electric Phoenix Nanotom S nano-CT scanner (voxel size = 0.01413 mm), and previously presented in Grine et al. (2019). Due to their larger size, elements of the KNM-ER 64061 postcranial skeleton were scanned using the General Electric Phoenix VTOMEX L240 micro-CT system (voxel size varied among elements, ranging from 0.03 to 0.07 mm). Volumetric renderings were computed using Avizo and VGStudioMax software, and new visualization of high-density regions unreported by Grine et al. (2019) are presented here.

3.2.2. Micro-X-ray fluorescence

Non-destructive chemical interrogation of the fossils was accomplished with a Bruker M4 Tornado benchtop micro-X-ray fluorescence (μXRF) spectrometer. X-rays generated from a rhodium tube excited to 50 kV with 400 μA current were focused via polycapillary optics onto samples in 2 mbar vacuum. Samples were rastered beneath the primary X-ray beam and fluorescent X-ray energy spectra were measured simultaneously on two 30 mm^2 silicon drift energy dispersive spectrometer (EDS) detectors. Fluorescent X-ray EDS spectra were assigned to 20 μm-wide pixels that had an average primary beam dwell time of 30–40 ms, but the sample surface area and volume interrogated depended on incident X-ray energy, sample surface roughness and height relative to beam focus, and sample density. Bruker software (Bruker M4 Tornado v. 1.6.621.0) was used to deconvolve fluorescent X-ray EDS spectra from background, emission line overlaps, and detector artifacts (i.e., pile-up peaks and detector escape peaks); develop corrected count sum spectra for regions of interest (ROI) and whole sample chemical images; and calculate standardless first-principles sample and ROI stoichiometric compositions. Data were output as chemical images of total counts in energy windows 87 % the width of corrected emission spectral line peaks and as element oxide abundances. Quantification of sum spectra on well-focused ROI resulted in less than 91 wt % oxide totals; because primary and altered biominerals often have significant quantities of hydrous or carbonate components not detectable by XRF, data were not normalized to 100 %. Accuracy and precision of quantification results depend on material properties and phase assemblages, which vary spatially even within ROI's, but are typically better than 20 % for light elements and 5–10 % for metals.

3.2.3. Synchrotron XRF and absorption spectroscopy

Two beamlines at the National Synchrotron Light Source II (NSLS-II) were used in this study for microanalysis of as-is samples (Supporting Information). The synchrotron beamlines are brighter X-ray sources than the benchtop μXRF, with smaller beams and tunable beam energy, permitting us to probe finer details and to quantify sample composition from sum spectra of smaller ROI's. Measured fluorescence of different elements is attenuated differently depending on, among other things, absorption by the matrix and thickness of the sample (which for these fossils is infinite). Mean fluorescence values for selected elements in each ROI were normalized by incident beam intensity. Raw counts were then converted into estimated element concentrations by correcting for attenuation and effective sampling depth, based on characteristic fluorescence energy and assuming a matrix of HAp. Thus uncertainty in absolute concentration, typically better than 10 % across a wide range of detectable concentrations, is much larger than the uncertainty in relative concentrations between similar samples measured with a given experimental setup.

Microbeam XRF maps at Beamline 8BM, the Tender Energy X-ray Absorption Spectroscopy and Imaging beamline (TES, Northrup, 2019) were run at 3449.5 eV with a 10 μm beam size. On-the-fly XRF maps used a 15 μm pixel size and 0.2 s/pixel dwell time, providing data on Mg, Al, Si, P, S, and Cl (via K fluorescence), Sr (L fluorescence) and U (M fluorescence). The XRF maps were used to select representative spots of the fossil material (avoiding fractures and surface contamination) for microbeam X-ray absorption near edge structure (XANES) analysis at the sulfur K edge (S-XANES) and uranium M_5 edge (U-XANES). Synchrotron-based XANES provides chemical information such as oxidation state and chemical speciation for the target element, at the microscale. In particular, S-XANES can differentiate organic and inorganic S species. XANES measurements are accomplished by scanning the incident beam energy across the element's absorption edge while collecting the element-specific fluorescence signal and assigning this signal into energy increments of 0.1 eV.

Beamline 4BM, the X-ray Fluorescence Microprobe (XFM), is the hard X-ray instrument co-developed with TES at NSLS-II. On-the-fly XRF maps were run at 18 keV with a 10 μm beam size, a 20 μm pixel size and 0.2 s/pixel. This beamline has 7 silicon drift EDS detectors, and the sum of all detectors for each pixel across these regions gives raw counts for

the ROIs. Accessible elements at XFM include transition metals and heavier elements via K and L fluorescences, for XRF and absorption spectroscopy.

4. Results

4.1. Sedimentology

Although many other vertebrate remains occurred on the surface and were recovered through careful scraping and screening of the outcrop surface (Fig. 3B, Supplemental Table 1), no additional hominin fossils were found *in situ* during excavation of Trench 7. Microstratigraphic description of the outcrops plus trenching revealed sedimentologic variability both vertically and lateral to the initial discovery location of the KNM-ER 64060 hominin teeth (Fig. 3). The teeth were excavated from a clayey siltstone unit 180 cm thick where the teeth were found (Fig. 3A–C, D). This clayey siltstone unit thins by about 100 cm towards the south-southwestern end of the excavation area and likely filled in an original topographic depression on the underlying fossiliferous silts. A sandy siltstone unit (about 15 cm thick) is interbedded with and overlies the tooth-bearing clayey siltstone unit.

The bedding contact between the tooth-bearing clayey siltstone and thin, overlying sandy siltstone is sharp but irregular, with a decimeter-scale indention interpreted as either a small scour or a cross-section of a vertebrate footprint. Pedogenic fabrics and bioturbation have obscured primary bedding structures in the sandy and clayey siltstone units. Lenses of *Bellamya*-bearing silty sand occur near the top of the clayey and sandy siltstones, which are capped by a well-cemented, tabular, *Bellamya*-bearing sandstone on a sharp depositional contact (Fig. 3).

Overall, the sediment composition and architecture of the different lithofacies, along with the presence of the aquatic gastropods above and below the hominin levels (Fig. 3), are evidence for a lake margin environment with relatively small-scale (e.g., 10's of m) lateral variation in depositional sub-environments. Crack fills, root traces, and soil development indicate temporary emergence as dry land, while the gastropod-bearing silty sands indicate recurring periods of submergence. All of these features fit a persistent, low angle lake margin environment subject to fluctuating lake levels, with local topographic relief up to about 1 m formed by shallow off-shore, beach, back-beach and on-shore sub-environments.

4.1.1. Particle size distribution

The majority of disaggregated rocks have a siltstone texture with varying amounts of sand and clay (Fig. 4A, Table 1). A particle size distribution curve of all rock samples is shown in Fig. 4B. Samples from locations 2, 4, 7, 8 and 10 all show similar particle size distribution curves, with a dominance of silt. This group includes sample 2 (from the trench at the level from which the KNM-ER 64060 teeth were excavated) and sample 4 (the top of trenched outcrop surface where the KNM-ER 64061 postcranial bones were discovered) (Fig. 3). The *Bellamya*-bearing sandstone (sample 6) has the coarsest texture (clayey, silty sandstone), followed by sample 9, a sandy siltstone that is the inferred source (see discussion below) of the KNM-ER 64061 postcranial bones prior to their exhumation and transport down the modern outcrop slope.

4.1.2. Sediment composition

Trace and major element composition of sediment samples from F25787–F25966 are tabulated in Supplemental Dataset 1. Strong fluorescence resulted in noisy XRD patterns that made mineral identification challenging. The clay fraction contains a mixture of smectite and interstratified smectite-illite minerals (rectorite).

4.2. Bone and tooth composition and chemical images

4.2.1. Nano-CT and micro-CT

Volumetric reconstructions of the nano-CT images indicate that most of the KNM-ER 64060 dentition exhibits high density areas that appear to be associated with cracks in the enamel and/or dentine, as demonstrated here for the LM_3 (Fig. 5a, b and Supplemental Video 1, 2) and the RP_4 (Fig. 5c and Supplemental Video 3, 4). (Supplementary videos related to this article can be found at https://doi.org/10.1016/j.quascirev.2024.108525). This bright phase also occurs as discrete patches on the surface of the roots, as demonstrated here for the LC (Fig. 5d). The high-density regions were associated with elevated Ba and S concentrations, semi-quantitatively suggesting barite ($BaSO_4$) accumulations when examined using a portable hand-held XRF analyzer (pXRF, Supplemental Information, Supplemental Dataset 2). Scanning electron microscopy-based EDS analysis (Supplemental Material) of the barium-sulfur deposit confirmed that the material is stoichiometric barite (Supplemental Fig. 2).

Postcranial elements comprising specimen KNM-ER 64061 were also imaged with micro-CT and exhibited high-density spots like those seen in the KNM-ER 64060 teeth (Fig. 5f). Examination by pXRF analyzer of the humerus and clavicle revealed more barium on the surfaces of both than a modern springbok parietal bone (Supplemental Dataset 2).

4.2.2. Benchtop μXRF

All tooth and bone samples are dominated by Ca and P, consistent with their origin as HAp. Different chemical elements were preferentially enriched in tooth enamel, dentin, or bone material, permitting differentiation and comparison of the specimens' histories. These results are summarized in Supplemental Fig. 3 and tabulated in Supplemental Dataset 3.

Aluminum and Si, likely from sediment matrix material or authigenic clay precipitation, are present at weight percent levels (Supplemental Fig. 3a). Dentin material from KNM-ER 64060 teeth collected at F25787 is enriched in S and U compared to levels of these elements in other

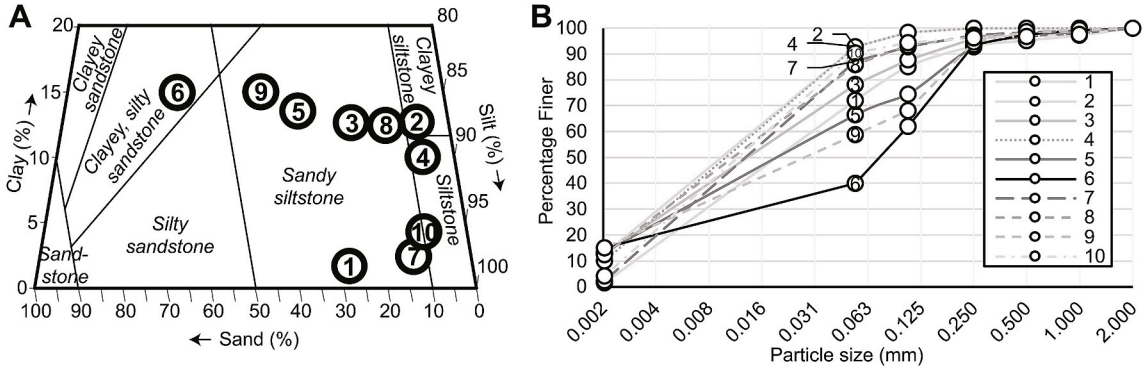

Fig. 4. (A) Sedimentary texture and (B) particle size distribution of disaggregated rock samples from F25787–F25966.

Fig. 5. Nano-CT reconstructions of KNM-ER 64060 teeth and micro-CT reconstruction of KNM-ER 64061 clavicle. (a) Orthoslice through the distal aspect of the LM_3. Denser regions are brighter. Scale = 2 mm. (b) Volumetric rendering of mesiobuccal view LM_3, together with a ghosted version highlighting the barite veins in the primary cracks in the tooth. Other large (wide) secondary cracks are devoid of barite. Scale bar = 5 mm. (c) Volumetric surface rendering of distobuccal view of RP_4, together with a ghosted version highlighting the barite veins in the primary cracks in the tooth. Unlike the LM_3 (b), at least one of the large secondary cracks contain barite deposits. Scale bar = 4 mm. (d) Volumetric surface rendering of distolingual view of LC, together with a ghosted version highlighting the high-density barite deposit on the distal surface of the root. Scale bar = 4.5 mm. (e) Photograph of clavicle fragment from KNM-ER 64061. (f) Micro-CT density rendering of a clavicle fragment from KNM-ER 64061, with brightest white pixels representing barite mineralization as determined by pXRF.

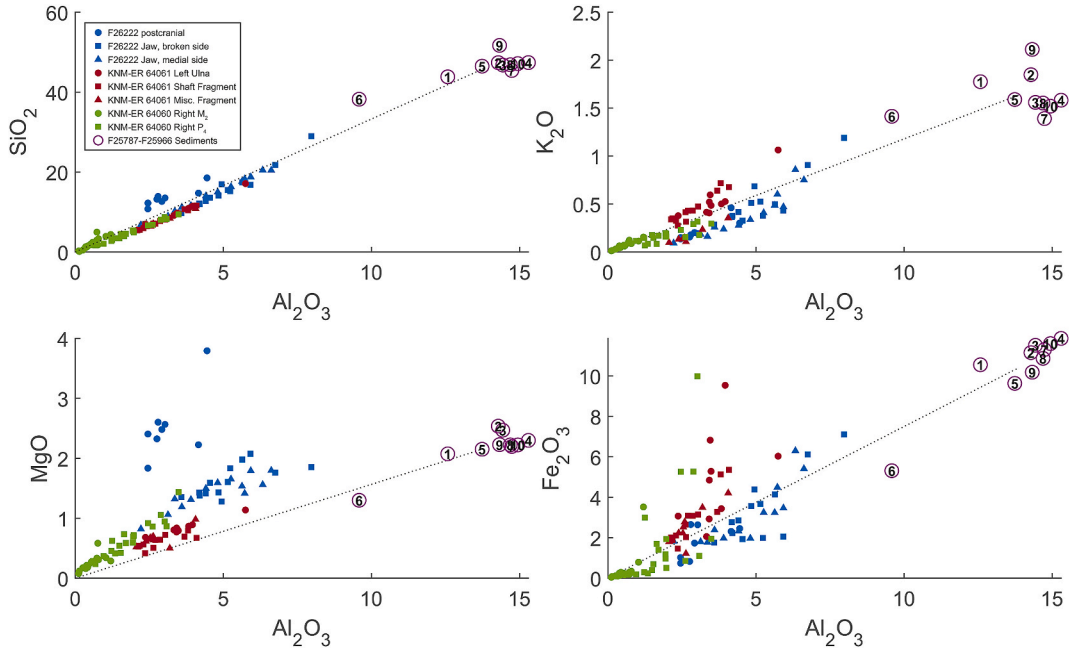

Fig. 6. Bi-plots of F25787–F25966 and F26222 specimens' μXRF quantification results from ROIs, reported as oxide weight percentage, showing admixture of low-Al, low-Si biogenic HAp with upper Burgi Member bulk sedimentary rocks from F25787–F25966 (circles). Deviations from mixing lines (shown in relation to the average sedimentary rock compositions) indicate other alteration, such as carbonate, oxide, or authigenic clay precipitation, or diffusion/exchange reactions.

materials, including dentin from the F26222 control site and KNM-ER 64061 postcranial bones from F25966 (Supplemental Fig. 3b). Tooth enamel from KNM-ER 64060 teeth has less Fe, Mn, Ba, Sr, Zr, and Cu, and more Zn than other materials (Supplemental Fig. 3b).

Two-element cross-plots were used to examine physical admixtures of fossil and matrix material and identify alteration end-members relative to bulk sedimentary rock compositions (Fig. 6). There are no systematic differences in sample alteration by locality. This is illustrated by several examples. First, all specimens from F25787–F25966 (KNM-ER 64060 and KNM-ER 64061) and the jaw fragment from F26222 have Si and Al contents that are well-explained by admixture of material of the upper Burgi Member sedimentary units exposed and excavated in F25787–F25966, but the postcranial fragment from the KBS Member at F26222 has elevated Si. Upper Burgi Member sediments explain K/Al variability of teeth from F25787 (KNM-ER 64060) and both the jaw and postcranial specimens from F26222, but not the postcranial bones from F25966 (KNM-ER 64061), which have elevated K. All cranial (tooth and jawbone) specimens from both F25787–F25966 and F26222 share a Mg/Al ratio that is higher than that of sediment samples at F25787–F25966, and postcranial bone specimens from F25966 (KNM-

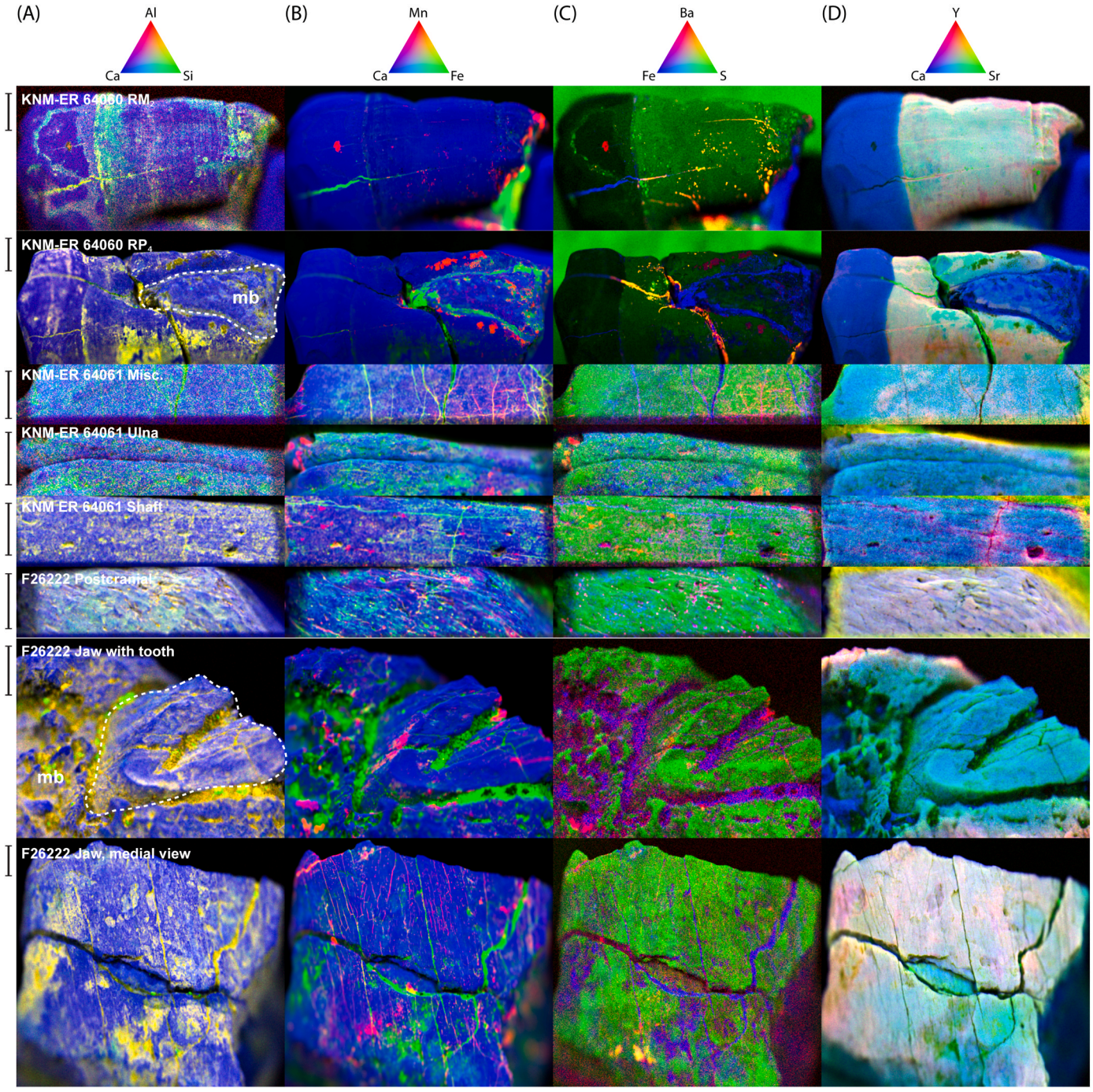

Fig. 7. Composite chemical images of specimens. All scale bars are 3 mm. Colors are scaled to the maximum concentration of each element in each sample. Dashed white lines delineate tooth material from mandibular bone (mb). (A) Al–Ca–Si. Note Si uptake along periradicular banding in KNM-ER 64060 RM_2. (B) Mn–Ca–Fe. (C) Ba–Fe–S. Note Ba on KNM-ER 64060 teeth is associated with both S (appears yellow) and Mn (appears red; compare to panel B). (D) Y–Ca–Sr. Note Y uptake along fractures and pits in KNM-ER 64061 Shaft, and compare to Y uptake only along outer jawbone found at F26222 but not along broken side of jawbone, and similarly only along outer postcranial bone found at F26222 but not along pits.

ER 64061) contain less Mg than postcranial bone specimens from F26222 with equivalent Al concentrations. On the other hand, some F25787–F25966 specimens have more Fe than F26222 specimens, and many have Fe/Al higher than that of F25787–F25966 sediments.

Chemical images of minor and trace element enrichments, coatings, and veins were used to develop a chemical taphonomic and alteration history of the specimens (Fig. 7). Plates with all chemical images are shown in Supplemental Figs. 4–11, and key features are discussed here.

Silicon is generally associated with Al (Fig. 7A), and likely represents detrital or authigenic clays (Kohn et al., 1999; Parker and Toots, 1970). In addition, Si alteration follows growth lines in tooth root dentin and irregular pockmarked veins in tooth enamel in KNM-ER 64060 specimens.

Manganese and Fe are present in thin, patchy coatings on samples,

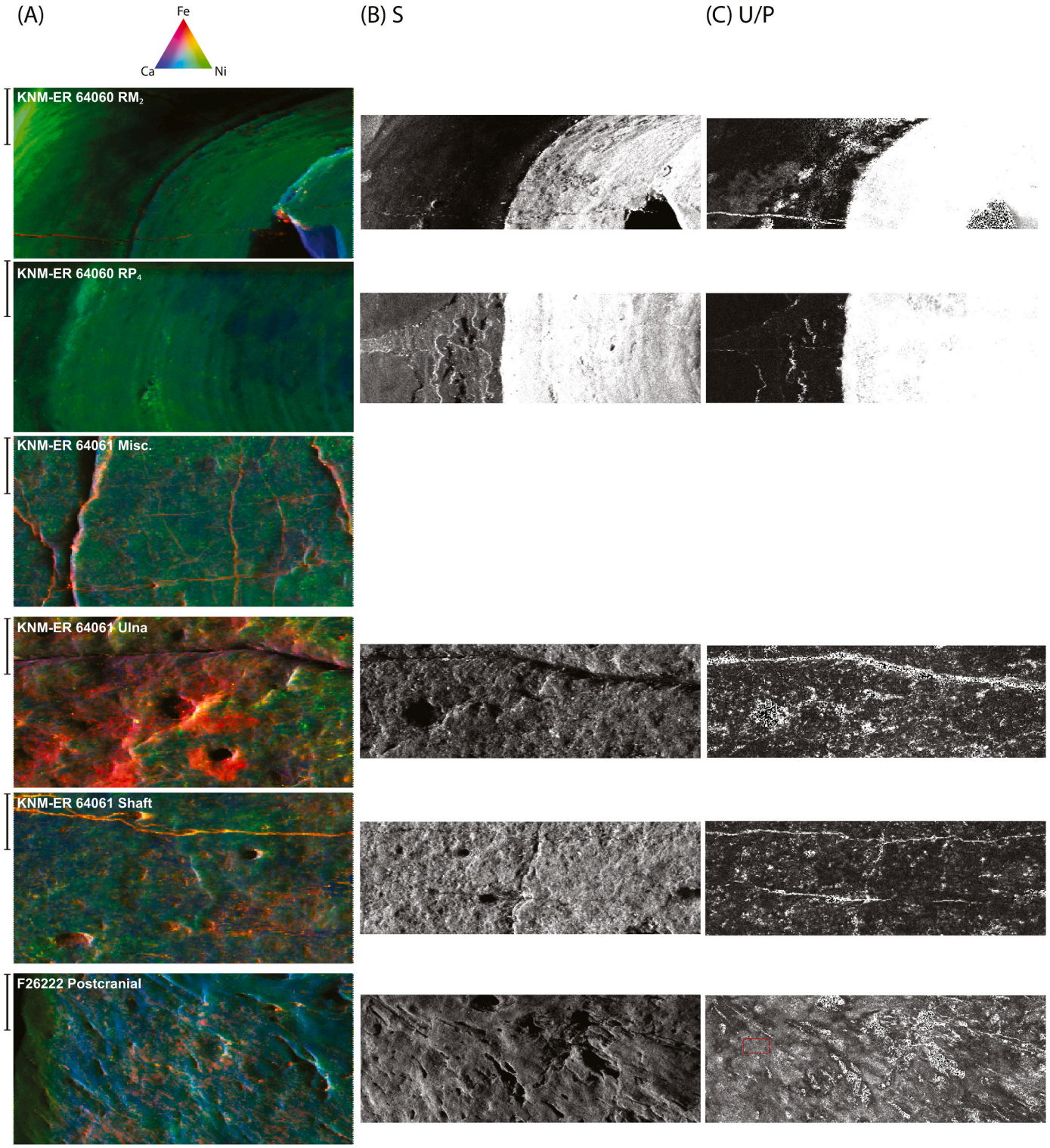

Fig. 8. Synchrotron XRF maps. Scale bar is 1 mm for all images. (A) Fe–Ni–Ca composite chemical image. Ni is fairly uniformly distributed in the apatite, while Fe is highly heterogeneous and significantly found coating fractures and surfaces. (B) Sulfur concentration maps from TES XRF data. Lighter shading is higher concentration; all images set to same absolute scale. (C) U/P maps from TES XRF data. Lighter shading is more U; all images set to same absolute scale.

and as oxides and silicate phases in fractures and holes (Fig. 7B). Different fractures contain either one or both of these redox-sensitive metals, suggesting that at least two phases of alteration occurred at different oxidation states interspersed by physical damage to the specimens. Specimens from all three sites (F25787–F25966 and F26222) also contain at least one fracture with no metal enrichment, suggesting continuation of physical alteration after chemical alteration, likely during exhumation.

Fractures and holes are also associated with Ba enrichments (Fig. 7C). In teeth and post-cranial specimens from F25787–F25966, Ba is often coincident with S enrichments and consistent with barite ($BaSO_4$) mineralization (Fig. 7C) where dense phases are observed in nano-CT volumetric reconstructions (Fig. 5a-d). In the KNM-ER 64060 teeth, barite mineralized the latest (more recent) fractures that lacked Fe and Mn enrichment. Barium is also present in regions on the KNM-ER 64060 teeth without S, instead associated with Mn (Fig. 7B and C). A small remnant of mandibular alveolar bone associated with the KNM-ER 64060 RP_4 tooth is enriched in Fe but not Ba, while a mandible fragment from F26222 is enriched in both elements (Fig. 7C).

Some elements, such as Y and Sr, are selectively incorporated into the imaged hominin specimens (Fig. 7D). These elements, which are compatible in HAp and inherited from modern or ancient porewaters (Hoppe et al., 2003; Nelson et al., 1986; Parker and Toots, 1970; Trueman and Tuross, 2002), are enriched in tooth dentin in KNM-ER 64060 specimens. Several other environmentally trace elements, including Ce, U, Nd, and La, have been concentrated into altered tooth dentin to up to several thousand parts per million (Supplemental Fig. 3B); these amounts are comparable to those seen in the outermost rim of fossil bones and teeth that concentrated these elements from soil waters, groundwaters, or other diagenetic fluids (Kohn et al., 1999; Millard and Hedges, 1996; Parker and Toots, 1970; Trueman et al., 2006; Trueman and Tuross, 2002). Porous remnant mandibular alveolar bone in RP_4 had comparably less Y and Sr than the dentin. In F25966 postcranial specimens (KNM-ER 64061), Y is preferentially incorporated along fractures, indicative of uptake following physical damage to the specimen (Fig. 7D). On the other hand, Y is preferentially incorporated into the exterior of the jawbone specimen from F26222, but not into broken jaw interior bone, broken tooth dentin or root material. This relationship suggests that Y was incorporated from pore fluids prior to jawbone breakage of the F26222 specimen.

4.2.3. Synchrotron XRF imaging and spectroscopy

Synchrotron XRF maps (Fig. 8A) from beamline XFM shows chemical heterogeneity associated with fractures and other alteration of primary fossil material, like those seen with benchtop μXRF. The concentrations of trace and minor elements in the best-preserved fossil material in areas free of cracks, pores, or adhered sediment are reported in Table 2.

Sulfur is fairly uniformly distributed in the fossil bone and enamel but highly enriched in the dentin (Fig. 8B). This S may originate from within the organism prior to death, as organic components as well as being structurally incorporated into the biomineral, or from the environment through interaction with fluids, microbial activity, or redox cycling. To address S chemical speciation, we measured microbeam S-XANES on several spots that were selected to be the most representative of the least-altered fossil material, not fractures or obviously highly enriched regions. These spectra (Fig. 9A) show that the majority of S is in the form of sulfate. For comparison, we measured S-XANES in a well-crystallized inorganic fluorapatite from Slyudyanka, Russia, that contains trace sulfate and a smaller amount of sulfite. The enamel S-XANES showed a spectrum similar to the reference apatite, with several spectral features corresponding to incorporation of sulfate into the crystal structure. The enamel also shows some sulfite incorporation, and, importantly, a small but definite component of organic sulfide species consistent with protein S.

Uranium is variably enriched in the bones, mostly along fracture surfaces, and in the teeth is highly enriched in the dentin and lowest in the enamel (Fig. 8C). U-XANES shows that the U is oxidized, present as U (VI) (Fig. 9B). This distribution is consistent with uptake from the environment over time, and possibly as a function of porosity (Hedges, 2002; Trueman and Tuross, 2002).

5. Discussion

5.1. Sedimentary history of hominin teeth and postcranial bones at F25787–F25966

Gathogo and Brown (2006) interpret the variously massive and bioturbated fine sandstone beds associated with siltstone with pedogenic structures as a marginal lacustrine facies association. Trenching and documentation by AKB revealed that, at F25787–F25966, these lithologies are arranged in a coarsening-upwards sequence of clayey siltstone overlain by sandy siltstone, and finally by well-sorted, cemented, *Bellamya*-bearing clayey, silty sandstone. This sequence is interpreted as transgressive, with the clayey siltstone representing a paleosol developed in a marginal lacustrine environment, possibly a temporarily subaerial lagoon; the sandy siltstone representing a back-beach or marginal lagoonal environment with less paleosol development; and *Bellamya*-bearing sandstones representing a foreshore or beach-face environment. The transgressive interval occurred over 10.5 vertical meters and an estimated time interval of *ca.*10 kyr based on generalized rates of sediment accumulation for the upper Burgi Member (Brown and McDougall, 2011). This could be part of a precessional cycle (21 kyr) controlling variability in regional precipitation, or part of a longer trend of increasing flow into the Omo-Turkana Basin resulting in lake expansion during deposition of the upper Burgi Member (Baldes et al., 2024; Trauth et al., 2005; Van Bocxlaer et al., 2008).

Microstratigraphy at F25787–F25966 documents the vertical and lateral relationships of different lithologies and their relationships to the surface scatter of KNM-ER 64061 and the *in situ* dentition of KNM-ER 64060 (Fig. 3). Critical considerations include: (1) close spatial and stratigraphic proximity of the hominin dental and postcranial remains; (2) excellent preservation of the postcranial bones (KNM-ER 60641) contrasted with absence of bone (except for minor mandibular alveolar bone remnants) but the survival of well-preserved, associated teeth with intact roots in KNM-ER 60640; (3) very restricted spatial dispersal in the paleosol of the associated *in situ* teeth, along with limited surface scatter of the postcranial bones; (4) occurrence of the postcranial bones on the outcrop surface, with the highest occurrence of these fossils about 1 m stratigraphic distance below the position of the *in situ* teeth in the paleosol; (5) presence of other well-preserved, fragmentary vertebrate

Table 2
Estimated element concentrations (ppm) from synchrotron XRF of well-preserved regions on fossil specimens.

	KNM-ER 64060			KNM-ER 64061			F26222
	RM_2 dentin	RP_4 dentin	RP_4 enamel	Left ulna	Shaft fragment	Misc. fragment	Postcranial bone fragment
Mn	1520	2200	600	8970	12700	11000	3150
Fe	1520	3580	1640	39100	18400	15300	6990
Ni	320	420	61	180	150	110	390
Cu	180	230	44	670	290	93	210
Zn	270	290	600	250	220	220	190
U	740	840	26	71	72	55	85

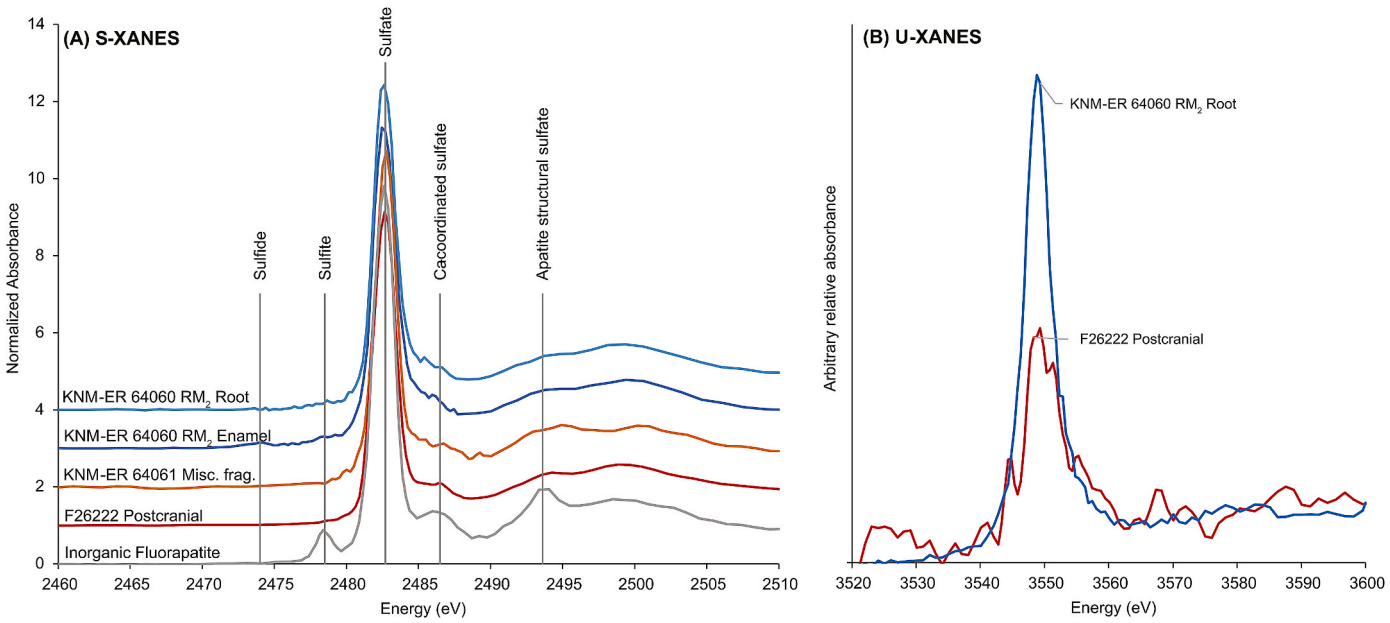

Fig. 9. TES XANES spectra of fossils. (A) S-XANES showing sulfate structurally incorporated in the apatite in all of the samples. Spectra are normalized to post-edge absorbance of 1 and are offset for comparison. (B) U-XANES showing peaks shifted to higher energy consistent with U(VI). Sample F26222 has much lower U concentration than sample KNM-ER 64060 (Table 2). Spectra are normalized to the same post-edge absorbance for comparison.

remains in the silty sands (Supplemental Table 1); and (6) absence of other vertebrate remains in the paleosol except for a single canine of a small carnivore.

Assuming that the fossils belonged to one individual, these features can be explained by different early post-mortem taphonomic histories involving rapid burial of the post-cranials at the same time as the nearby mandible disintegrated, either on the ground surface or buried in the upper soil. If the fossils represented two different individuals, then the different taphonomic histories might be more easily explained, but this requires spatial proximity of two sets of hominin remains that have no overlapping skeletal parts and belong to the same level of maturity and body size, and plausibly to the same species. In our opinion, the former interpretation is more likely, although it represents an unusual juxtaposition of different preservation states for a single individual in a lake margin depositional setting.

A parsimonious interpretation for the position and preservation of KNM-ER 64061 postcranial bones found on the F25787–F25966 ground surface, compared to the *in situ* KNM-ER 64060 teeth, is that the postcranial bones were buried soon after death by sandy siltstone in a shallow lake-margin environment next to the emergent surface represented by a paleosol. The succession of distinct sedimentary units, their inferred depositional environments, and the sequence of events involving this style of preservation of the hominin remains are reconstructed in Fig. 10.

The lateral dispersal of the postcranial bones and displacement from the dentition likely predated burial: after the hominin individual's death, its bones were scattered near the shoreline, with the mandible slightly farther from shore in clayey silt (Fig. 10A). Hominin remains that survived initial bone dissolution (postcranials) were preserved by rapid burial, but any others exposed on the paleosol surface (e.g., the mandible) were destroyed by scavenging, trampling, weathering (Behrensmeyer, 1978), and/or chemical dissolution through microbial osteolysis (Kendall et al., 2018; Turner-Walker, 2008) (Fig. 10B). Significant transport by water is unlikely given the close association of different skeletal elements (unless initially as an intact carcass) (Boaz and Behrensmeyer, 1976), but scavengers may have moved bones around the immediate death site and consumed some of the missing skeletal elements. The postcranial bone material did not dissolve post-burial in the sandy siltstone, possibly because this site remained slightly below the local water table.

Bones and teeth can be preserved in soils under specific biological, chemical, and physical conditions (Behrensmeyer, 1978; Retallack, 1988; Turner-Walker, 2008). Intact teeth with roots were released from the mandible to be buried in the soil. The vertical depth (43 cm) through which the KNM-ER 64060 teeth were scattered is explained by dislodgement from the mandible, a result of dissolution of the jawbone (either prior to or after shallow burial), and subsequent movement individually via bioturbation combined with pedogenic cracking of the silty clay (Fig. 10C), which is smectitic and expands easily. The mineralogy of the clay phase is dominated by swelling and interstratified clay minerals, accounting for the strong block structure of the clayey siltstone despite relatively low clay content. Swelling clays mix soils and the sedimentary particles—including fossils—within them (Yaalon and Kalmar, 1978). We hypothesize that, based on their shape differences, the single-rooted incisors and canines were reworked farther down into the soil by bioturbation and clay swelling-shrinking processes than the multi-rooted, blocky molars and premolars. Because the teeth were preserved in such a small volume of sediment, this is strong evidence that an intact mandible was stabilized on the land surface (e.g., by plant growth) prior to its disintegration on or in the upper soil layer.

After lake transgression (Fig. 10D) and burial (Fig. 10E), the surviving post-cranial bones weathered out as surficial lag from a source unit atop the clayey siltstone. They were then distributed downslope by recent erosion to more than 1 vertical m below the level of the *in situ* teeth (Fig. 10F). Note that if the postcranial bones had been subjected to the same surface processes that destroyed the mandible, they would not have survived as fossils; their excellent preservation requires protection from these processes, i.e., by early post-mortem burial.

5.2. *Preservation of primary hominin biominerals*

Fossilized biominerals under study represent a range of mineral-organic-volatile components and the interaction of the original biominerals in the living hominin with post-burial biogeochemical processes. The results of this study provide evidence for long-term retention of biomineral composition in different skeletal elements. Enamel is the hardest and richest in mineral HAp, composed of 95 % HAp and less than about 5 % organic matter (Cacciotti, 2016; Driessens and Verbeeck,

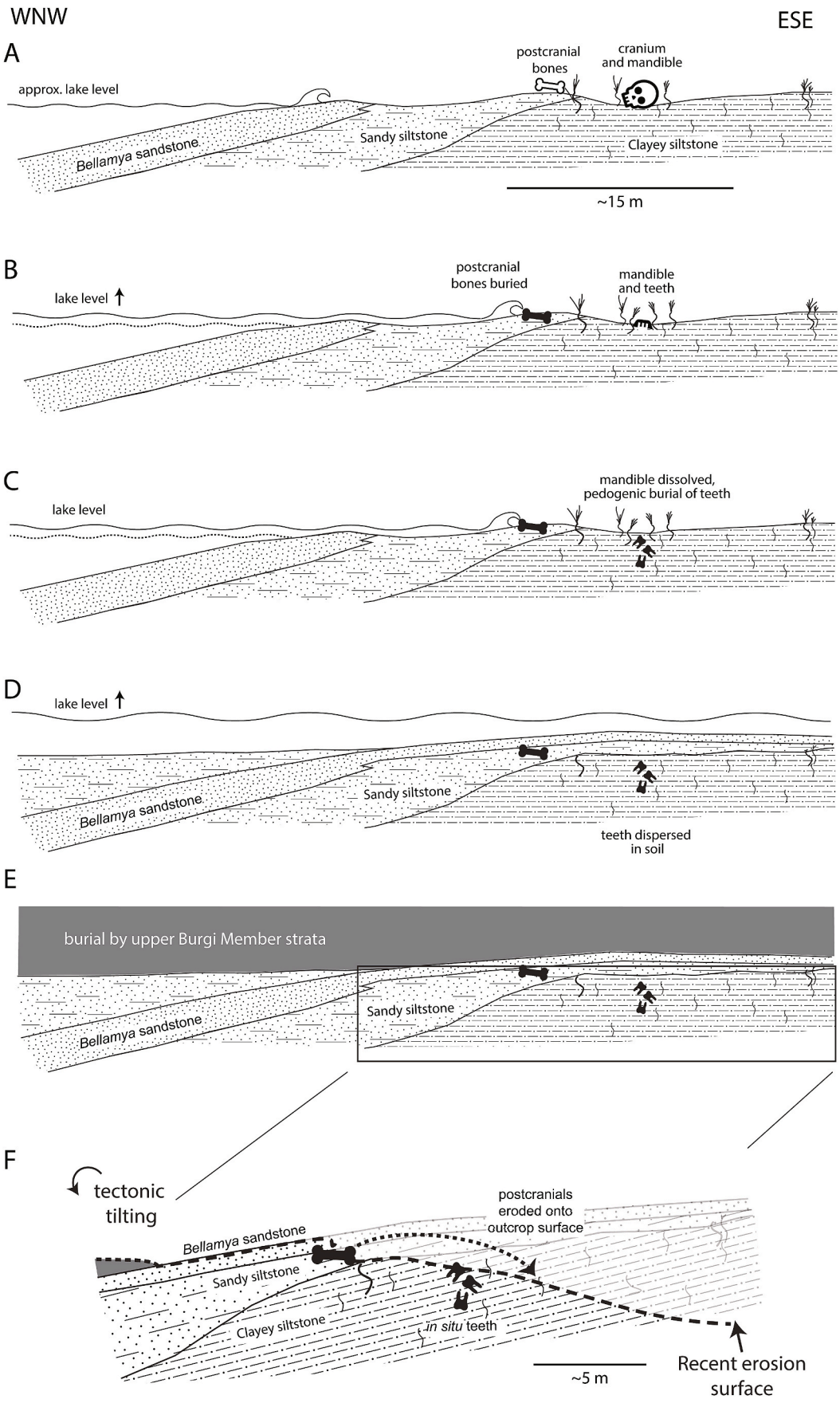

(caption on next page)

Fig. 10. Proposed depositional and physical taphonomic history at F25787–F25966 inferred from microstratigraphic relationships. (A) Alternating sandy and clayey silts deposited in a lake margin setting with local topographic relief; hominin death occurred at or near this location followed by scavenging. Postcranial bones disarticulated and dispersed several meters north and west of the associated mandible (possibly with cranium). (B) Lake margin processes rapidly buried the postcranial elements in sandy silt, while the mandible with full dentition was exposed on the adjacent soil surface and mandibular bone was gradually destroyed. (C) The teeth were incorporated into the soil, moving down from the surface by processes such as bioturbation, cracking, shrinking, and swelling of clays. (D) Lake transgression over a low-gradient shoreline buried the soil with sandy silt, then with the *Bellamya*-bearing sand, while postcranial elements remained buried in adjacent clayey silt deposits. (E) Lake transgression-regression cycles and fluvial-lacustrine deposition of upper Burgi Member and younger Koobi Fora Formation strata over the site. (F) Expanded view from (E) shows tilting 14°WNW, uplift, and erosion that exposed the hominin remains on the Recent outcrop surface. Postcranial bones eroded from the sandy siltstone onto this surface, and four teeth also eroded from the dentition buried in the paleosol. Compare to Fig. 3D; more details in text.

1990; Kendall et al., 2018). Bone is about 70 % HAp and 30 % organic matter (comprised mainly of collagen) (Driessens and Verbeeck, 1990). Dentin has the lowest mineral content at 55 % HAp with about 30 % organic matter and 15 % fluids (mainly water) (Driessens and Verbeeck, 1990). The degree of chemical exchange between each biomineral and diagenetic fluids tends to inversely vary with the proportion of mineral fraction (Hedges, 2002; Lambert et al., 1985; Trueman, 2013). Thus, enamel is typically the least susceptible to chemical alteration during diagenesis, and dentin the most (Kendall et al., 2018; Parker and Toots, 1980; Turner-Walker, 2008).

The fossils at both localities are physically well-preserved but have spatially heterogenous chemical alteration at micro-scale. They remain predominately HAp (Supplemental Fig. 12), and at the micron scale, primary biomaterial fabrics remain, including growth bands on tooth dentin highlighted by different uptake of various elements (e.g., Fig. 7). Sulfur-XANES analysis revealed several S coordination and oxidation states in the different biominerals in KNM-ER 64060 teeth (Fig. 9). Using the corrections for absorption cross section from Xia et al. (1998) and a fitting approach modified from Einseidl et al. (2007), the sulfur speciation in the enamel spot was 91 % sulfate, 5 % sulfite and 4 % organic sulfide. By comparison, sulfur in the reference inorganic apatite was 91 % sulfate and 9 % sulfite. Further quantification of a feature at 2493.5 eV that results from incorporation of sulfate into the apatite structure, and comparison of its intensity to that in the reference apatite, shows that 78 % of the sulfate in the enamel is structurally incorporated in apatite. A second feature, at 2486 eV, is common to sulfate chemically bound to Ca in some form (including incorporated into apatite). Intensity of this feature indicates that at least another 9 % of the sulfate is bonded to Ca, likely via adsorption on surfaces or grain boundaries. The remaining 13 % of the sulfate may be loosely bound or associated with the organic component.

Per expectation from primary biomineral composition, the best-preserved regions of fossil enamel have the lowest metal concentrations detected by synchrotron and benchtop XRF, with the least metal contamination in tooth enamel (Table 2, Supplemental Fig. 3, Supplemental Fig. 12). However, none of these metal concentrations are interpreted as primary biomineral concentrations.

5.3. Chemical alteration of hominin biominerals

In addition to matrix contamination, biominerals uptake elements from pore fluids (Lambert et al., 1985; Parker and Toots, 1970; Trueman and Tuross, 2002). The composition of a fossil may change via authigenic mineral precipitation in both primary or secondary pores, via diffusive ion exchange of the primary biomineral, or via primary biomineral dissolution and reprecipitation with a different composition (Kohn et al., 1999; Millard and Hedges, 1996; Trueman and Tuross, 2002). All fossil samples from F25787–F25966 and F26222 have less P and variable Ca compared to pristine biominerals, and tooth enamel samples are less altered than bone, which is less altered than dentin (Supplemental Fig. 12). While alteration trends depend on biomineral type, the style of incorporation of each element appears similar. A

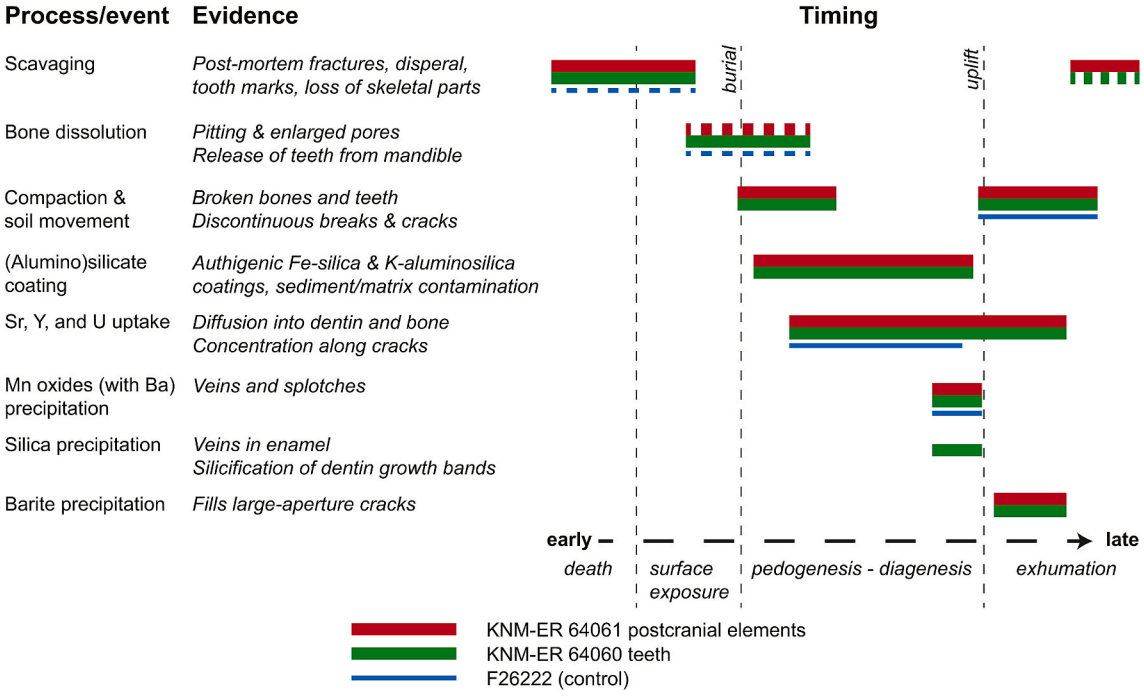

Fig. 11. Inferred alteration history of fossils constructed from cross-cutting relationships between chemical enrichments. Dashed horizontal bars indicate less intense or ambiguous effects of taphonomic processes.

summary paragenesis for the fossils' histories is shown in Fig. 11 and the nondestructive observations used to produce this history, integrated with the sedimentary history, are discussed below.

Benchtop μXRF data indicates that all specimens were contaminated by aluminous matrix material with compositions within the range of upper Burgi Member sedimentary units sampled at F25787–F25966 (Fig. 6). In addition, postcranial bones had slightly elevated K and Fe, and all specimens had elevated Mg. These elevated K and Fe concentrations were inconsistent with the bulk K/Al or Fe/Al ratios of all measured sediments. Therefore, these may be low-Al authigenic phases like alkali clays or iron smectites (e.g., nontranite or saponite), which precipitated on the specimens during diagenesis, locally concentrating these cations (Kohn et al., 1999; Parker and Toots, 1970). Although Mg was difficult to image (Supplementary Figs. 4–11), the shared Mg/Al ratio for all cranial specimens from both F26222 and F25787–F25966 is evidence for authigenic precipitation of a magnesium clay phase. Low Mg/Al phases in KNM-ER 64061 postcranial bones at F25787–F25966 and high Mg/Al phases in postcranial bones from F26222 may reflect locally variable pH or dissolved silica contents of groundwaters, which controls the aluminum content of authigenic clays (Birsoy, 2002; Francis et al., 2020). While the reasons for non-systematic incorporation of Mg into the samples are unclear, Mg variability among control specimens from F26222 indicates that variable Mg incorporation into KNM-ER 64060 and KNM-ER 64061 does not preclude those fossils deriving from the same individual.

Metals that are unlikely to replace stoichiometric components in HAp, such as Fe and Mn, are more likely to track secondary mineral precipitation (Kohn et al., 1999; Parker and Toots, 1970; Trueman and Tuross, 2002). Benchtop and synchrotron chemical images show that Fe enrichments trace rims of solution-enlarged pores and borings in bones and follow early fractures in bones and teeth (Fig. 7C; Fig. 8A and B; Fig. 9A). Thus, authigenic oxides and clays were incorporated into all samples after initial scavenging, dissolution of the mandible during surface exposure and soil development, and initial compaction associated with burial that cracked the fossils (Fig. 11). Tooth enamel samples host less of these elements than the other biomineral samples, which may be due to the more porous structure and lower HAp content of bones and dentin. Among dentin and bone samples, Mn tends to be lower in samples from F26222 than from F25787–F25966, suggesting that pore- and fracture-filling diagenesis at F26222 occurred under different redox conditions than the lake margin environment at F25787–F25966 (Supplemental Fig. 3).

Barite (Figs. 5 and 7) was found in a subsequent suite of fractures that cross-cuts earlier cracks and was found coating the KNM-ER 64060 teeth and KNM-ER 64061 bones. Together, this demonstrates a shared diagenetic history by the time sediments were exposed to sulfate-rich fluids following burial compaction and exhumation (Fig. 11). Barium enrichment was associated both with Mn-oxide coatings and with sulfate as barite (Fig. 7C), suggesting that later oxidizing fluids were variably sulfur-rich. In low-sulfate conditions (i.e., sulfidic or low total sulfur), Ba may concentrate in suitable habitats for microorganisms created by the increased sorption of water and nutrients by clays (Brock-Hon et al., 2012; Clarke et al., 2016), or the microbial reduction of sulfate under anaerobic conditions (e.g., McCready and Krouse, 1980). Taken together, the teeth and bones at F25787–F25966 appear to have shared aluminous contaminants from a generally similar depositional and burial environment, experienced similar authigenic clay precipitation following early bone dissolution and fracturing during burial compaction, and then a younger period of specimen cracking was followed by barite enrichment in all samples (Fig. 11).

Strontium is present in low amounts (0.02–0.04 wt %, Cacciotti, 2016) in pristine biominerals and U is metabolically excluded due to its toxicity to most fauna. Strontium (Fig. 7D) and U(VI) (Fig. 9B) can replace Ca in apatite (e.g., Clarke and Altschuler, 1958; Rakovan et al., 2002) and these should increase with increased alteration of primary material (Millard and Hedges, 1996; Nelson et al., 1986). Yttrium and other rare earth elements behave similarly (Kohn et al., 1999; Parker and Toots, 1980; Trueman and Tuross, 2002; Tütken et al., 2008). As expected, dentin is the most enriched in these trace elements (Fig. 7D and Fig. 8C). Enrichment of Sr, Y, and U in both dentin and fractures in the teeth suggest that dentin alteration is related to the chemical composition of the fluids infiltrating fractures (Fig. 7D), and that uptake of these elements was coincident with sample breakage during early burial and compaction at F25787 (Fig. 11). Enamel is the least altered and the least enriched in these elements. In addition, Sr, U, and Y clearly are incorporated into exterior mandibular bone material from F26222, but not into broken bone faces or dentin exposed by breakage. This indicates that physical damage and breakage of samples from F26222 postdated uptake of these elements from the paleosol or burial environment; this integration of physical and chemical taphonomies reveals a clear distinction between samples from different localities and time periods (Fig. 11).

The differences in sample alteration discussed above are closely related to primary biomineral composition, but samples derived from excavated or surface fossils of the upper Burgi Member at F25787–F25966 share parts of their taphonomic histories that are distinct from samples derived from the KBS Member at F26222 (Fig. 11). Specifically, following pre-burial and pedogenic dissolution of bone material, differences in altered biomineral composition between the KNM-ER 64060 teeth and the KNM-ER 64061 postcranial bones are better attributed to differences in the primary biomineral composition than to different diagenetic histories after burial.

5.4. Differential preservation of remains of single hominin individuals

The fact that the dental elements of KNM-ER 64060 are well preserved and largely lack associated mandibular bone indicates that the latter was largely dissolved, resulting in periradicular alveolar bone loss that would have enabled the tooth roots to become dislodged. This degree of mandibular osteolysis stands in contrast to the well-preserved cortical and trabecular bone of the KNM-ER 64061 postcranial elements. If these remains are from the same individual, as we infer, this means that the mandible and postcranial remains experienced different early post-mortem and/or post-burial diagenetic pathways. In the preceding discussion, we conclude that the primary difference was early burial of postcranial bones in marginal lacustrine sandy silt, but longer exposure of mandibular bone to surficial and pedogenic processes in nearby clayey silt. If KNM-ER 64060 and KNM-ER 64061 represent teeth and postcranial bones from the same associated partial skeleton, then this is only the fourth such skeleton with affinities to *H. habilis* (Fig. 12).

The association of isolated teeth with postcranial bones attributed to the same individual is unusual but not unknown in the Pleistocene hominin fossil record of eastern Africa. An important example includes the OH 80 teeth and postcranial remains attributed to *Paranthropus boisei* that were recovered *in situ* in the BK site of Olduvai Gorge (Domínguez-Rodrigo et al., 2013). Eight dental elements—two of which are attached to small fragments of mandibular alveolar bone—were excavated along with the relatively unweathered diaphysis of the right femur, the distal portion of the left humerus shaft, the proximal half of the right radius, and a fragment of tibial midshaft (Domínguez-Rodrigo et al., 2013). Another such association is provided by dentate, intact right mandibular corpus and isolated left mandibular teeth of specimen SAM-AP 6223 from the Middle Stone Age deposits of Klasies River Main Site, South Africa. The right corpus of this jaw preserves RP_4-M_2 in place, while the LP_4, LM_2 and LM_3 are isolated teeth with fully intact roots and no alveolar bone. The isolated LM_1 has a tiny fragment of alveolar bone adhering to the buccal surface of the roots (Grine, 2012; Grine et al., 2021). Like OH 80 and SAM-AP 6223, some of the dental elements of KNM-ER 64060 include adherent mandibular alveolar bone (Fig. 2B).

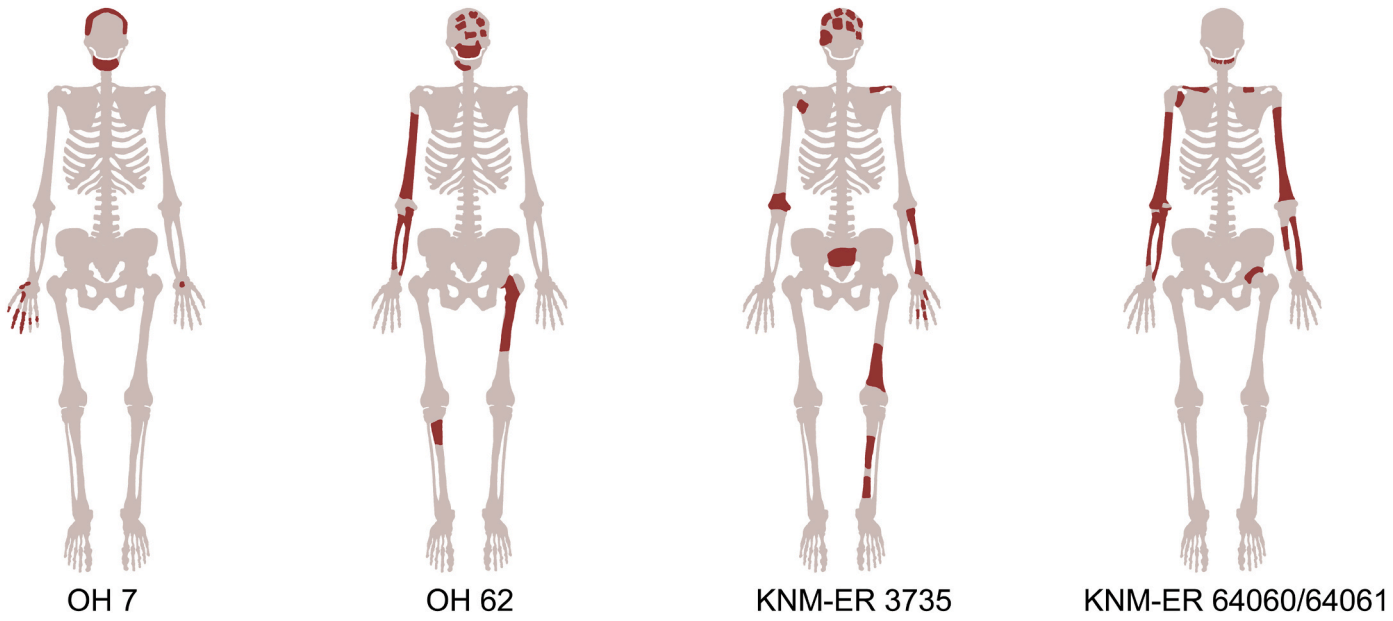

Fig. 12. *Homo habilis* specimens with both postcranial and craniodental elements. OH 7 is regarded by us as a probable association, whereas OH 62 and KNM-ER 3735 are regarded as comprising definite associations of such elements. If the KNM-ER 64060 teeth and KNM-ER 64061 postcranial bones are from the same individual, it would be the fourth such specimen known with affinity to *H. habilis*.

6. Conclusions

Nano-CT, micro-CT, and benchtop and synchrotron XRF were used here to examine the cross-cutting relationships between chemical signatures and ordinate the diagenetic taphonomic history of hominin fossils, an approach infrequently applied to hominin fossils (Dal Sasso et al., 2014; Kinyua et al., 1991; Trueman et al., 2006). A key advantage of these X-ray techniques is the ability to obtain chemical information non-destructively, without suffering beam damage or necessitating invasive sample preparation required for laser ablation, electron microscopy, or other potentially destructive microanalyses. The data were related to bulk characterization of sediment composition in the F25787–F25966 and F26222 localities. However, key differences in the sediment composition and detailed understanding of mineralogical controls on chemical uptake on fossils were limited by the X-ray techniques, which have 10 μm-scale or larger spatial resolution and fail to identify light elements such as carbon, nitrogen, oxygen, and sodium important in carbonate and nitrate minerals in the sediment.

Microstratigraphic relationships at the F25787–F25966 site indicate that the hominin postcranial (KNM-ER 64061) and the teeth with affinity to *H. habilis* (KNM-ER 64060) were preserved in slightly different but closely related, contemporaneous lake margin lithofacies. Lake transgression near the time of the individual's demise preserved the postcranial bones in lake margin sandy siltstone, while pedogenic processes dissolved nearly all mandibular bone and mixed the teeth through nearby clayey siltstones. Geochemical characteristics of sediments, paleosol, and fossil teeth and postcranial bones are consistent with their primary association as a single individual, representing only the fourth such specimen that is attributable to the species *Homo habilis* (Fig. 12). Verification that the teeth and postcranial bones are derived from a single individual is important because it permits unique insights about hominin morphology and ontogeny and broadens understanding of early hominin evolution.

Declaration of competing interest

The authors declare the following financial interests/personal relationships which may be considered as potential competing interests: Theodore M. Present reports financial support was provided by Simons Foundation. Ryan Tappero reports financial support and administrative support were provided by US Department of Energy. Catherine Clarke reports financial support was provided by South Africa Department of Science and Innovation. Paul Northrup reports financial support was provided by National Science Foundation. Paul Northrup reports financial support was provided by NASA.

Data availability

All data is available in the Supplementary Material and archived at https://doi.org/10.17605/OSF.IO/H8GUC

Acknowledgments

We gratefully acknowledge the Kenyan Ministry of Gender, Culture, the Arts and Heritage; the Kenyan National Commission for Science, Technology, and Innovation; and the National Museums of Kenya. L. Leakey obtained the permits from the Kenyan Ministry of Gender, Culture, the Arts and Heritage for the transport of the hominin fossils and sediments for chemical composition analysis in 2019. Cyprian Nyete collected sedimentary rock samples from the excavation area. T. Present was partially supported by Simons Foundation Grant 668346. Portions of this research were performed at the Tender Energy Spectroscopy (TES) and the X-ray Fluorescence Microprobe (XFM) beamlines and used resources of the National Synchrotron Light Source II, a U.S. Department of Energy (DOE) Office of Science User Facility operated by Brookhaven National Laboratory under Contract No. DE-SC0012704. Construction of, and work at the TES Beamline was partly funded by the National Science Foundation, Earth Sciences (EAR-1128957), NASA (NNX13AD12G) and the Department of Energy, Geosciences (DE-FG02-12ER16342). Benchtop μXRF data was acquired in the Caltech GPS Division Analytical Facility with the support of Chi Ma and John Grotzinger, with partial support from the Simons Foundation. E. Niespolo was supported by a Barr Postdoctoral Fellowship (Caltech). Sediment analyses were performed at the Stellenbosch University BIOGRIP node, which is funded by the Department of Science and Innovation of South Africa.

Appendix A. Supplementary data

Supplementary data to this article can be found online at https://doi.org/10.1016/j.quascirev.2024.108525.

References

Baldes, M.J., Raynolds, R.G.H., Feibel, C.S., 2024. The Upper Burgi Unconformity: a major hiatus in the fossiliferous Koobi Fora formation identified in area 116, east Turkana, Kenya. J. Afr. Earth Sci. 210, 105135 https://doi.org/10.1016/j.jafrearsci.2023.105135.

Behrensmeyer, A.K., 1978. Taphonomic and ecologic information from bone weathering. Paleobiology 4, 150–162. https://doi.org/10.1017/S0094837300005820.

Behrensmeyer, A.K., 1970. New hominid remains and early artefacts from northern Kenya: Preliminary geological interpretation of a new hominid site in the Lake Rudolf basin. Nature 226, 225–226. https://doi.org/10.1038/226225a0.

Birsoy, R., 2002. Formation of sepiolite-palygorskite and related minerals from solution. Clay Clay Miner. 50, 736–745.

Boaz, N.T., Behrensmeyer, A.K., 1976. Hominid taphonomy: transport of human skeletal parts in an artificial fluviatile environment. Am. J. Phys. Anthropol. 45, 53–60. https://doi.org/10.1002/ajpa.1330450107.

Brock-Hon, A.L., Robins, C.R., Buck, B.J., 2012. Micromorphological investigation of pedogenic barite in Mormon Mesa petrocalcic horizons, Nevada USA: implication for genesis. Geoderma 179– 180, 1–8. https://doi.org/10.1016/j.geoderma.2012.02.012.

Brown, F.H., Feibel, C.S., 1986. Revision of lithostratigraphic nomenclature in the Koobi Fora region, Kenya. J. Geo. Soc. 143, 297–310. https://doi.org/10.1144/gsjgs.143.2.0297.

Brown, F.H., McDougall, I., 2011. Geochronology of the Turkana depression of northern Kenya and southern Ethiopia. Evol. Anthropol. Issues News Rev. 20, 217–227. https://doi.org/10.1002/evan.20318.

Cacciotti, I., 2016. Cationic and anionic substitutions in hydroxyapatite. In: Antoniac, I. V. (Ed.), Handbook of Bioceramics and Biocomposites. Springer International Publishing, Cham, pp. 145–211. https://doi.org/10.1007/978-3-319-12460-5_7.

Clarke, C.E., Majodina, T.O., du Plessis, A., Andreoli, M.A.G., 2016. The use of X-ray tomography in defining the spatial distribution of barite in the fluvially derived palaeosols of Vaalputs, Northern Cape Province, South Africa. Geoderma 267, 48–57. https://doi.org/10.1016/j.geoderma.2015.12.011.

Clarke, R.S., Altschuler, Z.S., 1958. Determination of the oxidation state of uranium in apatite and phosphorite deposits. Geochem. Cosmochim. Acta 13, 127–142. https://doi.org/10.1016/0016-7037(58)90044-9.

Connors, K., Raynolds, R., 2022. Compiled Lake Turkana Stratigraphy Map.

Dal Sasso, G., Maritan, L., Usai, D., Angelini, I., Artioli, G., 2014. Bone diagenesis at the micro-scale: bone alteration patterns during multiple burial phases at Al Khiday (Khartoum, Sudan) between the Early Holocene and the II century AD. Palaeogeogr. Palaeoclimatol. Palaeoecol., Bone and enamel diagenesis: from the crystal to the environment - a tribute to Jean-François Saliège 416, 30–42. https://doi.org/10.1016/j.palaeo.2014.06.034.

Domínguez-Rodrigo, M., Pickering, T.R., Baquedano, E., Mabulla, A., Mark, D.F., Musiba, C., Bunn, H.T., Uribelarrea, D., Smith, V., Diez-Martin, F., Pérez-González, A., Sánchez, P., Santonja, M., Barboni, D., Gidna, A., Ashley, G., Yravedra, J., Heaton, J.L., Arriaza, M.C., 2013. First partial skeleton of a 1.34-million-year-old *Paranthropus boisei* from bed II, Olduvai Gorge, Tanzania. PLoS One 8, e80347. https://doi.org/10.1371/journal.pone.0080347.

Driessens, F.C.M., Verbeeck, R.M.H. (Eds.), 1990. Biominerals. CRC Press, Boca Raton.

Du Plessis, A., Roux, le S.G., Guelpa, A., 2016. The CT Scanner Facility at Stellenbosch University: an open access X-ray computed tomography laboratory. Nuclear Instrument. Methods Phys. Res. Sec. B-beam Interact. Mat. Atoms 384, 42–49.

Einsiedl, F., Schäfer, T., Northrup, P., 2007. Combined sulfur K-edge XANES spectroscopy and stable isotope analyses of fulvic acids and groundwater sulfate identify sulfur cycling in a karstic catchment area. Chem. Geol. 238, 268–276. https://doi.org/10.1016/j.chemgeo.2006.11.014.

France, C.A.M., Sugiyama, N., Aguayo, E., 2020. Establishing a preservation index for bone, dentin, and enamel bioapatite mineral using ATR-FTIR. J. Archaeol. Sci.: Report 33, 102551. https://doi.org/10.1016/j.jasrep.2020.102551.

Francis, M.L., Majodina, T.O., Clarke, C.E., 2020. A geographic expression of the sepiolite-palygorskite continuum in soils of northwest South Africa. Geoderma 379, 114615. https://doi.org/10.1016/j.geoderma.2020.114615.

Gathogo, P.N., Brown, F.H., 2006. Stratigraphy of the Koobi Fora Formation (Pliocene and Pleistocene) in the Ileret region of northern Kenya. J. Afr. Earth Sci. 45, 369–390. https://doi.org/10.1016/j.jafrearsci.2006.03.006.

Gee, G.W., Bauder, J.W., 1986. Particle size analysis. In: Methods of Soil Analysis. Part A, Madison, Wisconsin, pp. 383–411.

Grine, F.E., 2012. Observations on Middle Stone Age human teeth from Klasies River Main site, South Africa. J. Hum. Evol. 63, 750–758. https://doi.org/10.1016/j.jhevol.2012.08.005.

Grine, F.E., Gonzalvo, E., Rossouw, L., Holt, S., Black, W., Braga, J., 2021. Variation in Middle Stone Age mandibular molar enamel-dentine junction topography at Klasies River Main Site assessed by diffeomorphic surface matching. J. Hum. Evol. 161, 103079 https://doi.org/10.1016/j.jhevol.2021.103079.

Grine, F.E., Leakey, M.G., Gathago, P.N., Brown, F.H., Mongle, C.S., Yang, D., Jungers, W.L., Leakey, L.N., 2019. Complete permanent mandibular dentition of early *Homo* from the upper Burgi Member of the Koobi Fora Formation, Ileret, Kenya. J. Hum. Evol. 131, 152–175. https://doi.org/10.1016/j.jhevol.2019.03.017.

Grine, F.E., Mongle, C.S., Fleagle, J.G., Hammond, A.S., 2022. The taxonomic attribution of African hominin postcrania from the Miocene through the Pleistocene: associations and assumptions. J. Hum. Evol. 173, 103255 https://doi.org/10.1016/j.jhevol.2022.103255.

Hedges, R.E.M., 2002. Bone diagenesis: an overview of processes. Archaeometry 44, 319–328. https://doi.org/10.1111/1475-4754.00064.

Hoppe, K.A., Koch, P.L., Furutani, T.T., 2003. Assessing the preservation of biogenic strontium in fossil bones and tooth enamel. Int. J. Osteoarchaeol. 13, 20–28. https://doi.org/10.1002/oa.663.

Isaac, G.Ll, Leakey, R.E.F., Behrensmeyer, A.K., 1971. Archeological traces of early hominid activities, east of Lake Rudolf, Kenya. Science 173, 1129–1134. https://doi.org/10.1126/science.173.4002.1129.

Joordens, J.C.A., Dupont-Nivet, G., Feibel, C.S., Spoor, F., Sier, M.J., van der Lubbe, J.H. J.L., Nielsen, T.K., Knul, M.V., Davies, G.R., Vonhof, H.B., 2013. Improved age control on early *Homo* fossils from the upper Burgi Member at Koobi Fora, Kenya. J. Hum. Evol. 65, 731–745. https://doi.org/10.1016/j.jhevol.2013.09.002.

Kendall, C., Eriksen, A.M.H., Kontopoulos, I., Collins, M.J., Turner-Walker, G., 2018. Diagenesis of archaeological bone and tooth. Palaeogeogr. Palaeoclimatol. Palaeoecol. 491, 21–37. https://doi.org/10.1016/j.palaeo.2017.11.041.

Kinyua, A.M., Plummer, T., Shimizu, N., Melson, W., Potts, R., 1991. Provenance of Kanjera fossils by X-ray fluorescence and ion microprobe analyses. Adv. X Ray Anal. 35, 1165–1173. https://doi.org/10.1154/S0376030800013458.

Kohn, M.J., Schoeninger, M.J., Barker, W.W., 1999. Altered states: effects of diagenesis on fossil tooth chemistry. Geochem. Cosmochim. Acta 63, 2737–2747. https://doi.org/10.1016/S0016-7037(99)00208-2.

Lambert, J.B., Vlasak, S., Simpson, Szpunar, C.B., Buikstra, J.E., 1985. Bone diagenesis and dietary analysis. J. Hum. Evol. 14, 477–482. https://doi.org/10.1016/S0047-2484(85)80026-9.

Leakey, M.G., Leakey, R.E. (Eds.), 1978. Koobi Fora Volume 1: the Fossil Hominids and an Introduction to Their Context. Clarendon Press, Oxford.

Leakey, R.E.F., 1970. New hominid remains and early artefacts from northern Kenya: fauna and artefacts from a new Plio-Pleistocene locality near Lake Rudolf in Kenya. Nature 226, 223–224. https://doi.org/10.1038/226223a0.

McCready, R.G.L., Krouse, H.R., 1980. Sulfur isotope fractionation by *Desulfovibrio vulgaris* during metabolism of $BaSO_4$. Geomicrobiol. J. 2, 55–62. https://doi.org/10.1080/01490458009377750.

McDougall, I., Brown, F.H., 2006. Precise $^{40}Ar/^{39}Ar$ geochronology for the upper Koobi Fora Formation, Turkana Basin, northern Kenya. J. Geol. Soc. 163, 205–220. https://doi.org/10.1144/0016-764904-166.

Millard, A.R., Hedges, R.E.M., 1996. A diffusion-adsorption model of uranium uptake by archaeological bone. Geochem. Cosmochim. Acta 60, 2139–2152. https://doi.org/10.1016/0016-7037(96)00050-6.

Morley, M.W., Moffat, I., Kotarba-Morley, A.M., Hernandez, V.C., Zerboni, A., Herries, A. I.R., Joannes-Boyau, R., Westaway, K., 2023. Why the geosciences are becoming increasingly vital to the interpretation of the human evolutionary record. Nat Ecol Evol 7, 1971–1977. https://doi.org/10.1038/s41559-023-02215-5.

Nelson, B.K., Deniro, M.J., Schoeninger, M.J., De Paolo, D.J., Hare, P.E., 1986. Effects of diagenesis on strontium, carbon, nitrogen and oxygen concentration and isotopic composition of bone. Geochem. Cosmochim. Acta 50, 1941–1949. https://doi.org/10.1016/0016-7037(86)90250-4.

Northrup, P., 2019. The TES beamline (8-BM) at NSLS-II: tender-energy spatially resolved X-ray absorption spectroscopy and X-ray fluorescence imaging. J. Synchrotron Radiat. 26, 2064–2074. https://doi.org/10.1107/S1600577519012761.

Parker, R.B., Toots, H., 1980. Trace elements in bones as paleobiological indicators. In: Behrensmeyer, A.K., Hill, A.P. (Eds.), Fossils in the Making: Vertebrate Taphonomy and Paleoecology. The University of Chicago Press, Chicago, pp. 197–207.

Parker, R.B., Toots, H., 1970. Minor elements in fossil bone. GSA Bulletin 81, 925–932. https://doi.org/10.1130/0016-7606(1970)81[925:MEIFB]2.0.CO;2.

Rakovan, J., Reeder, R.J., Elzinga, E.J., Cherniak, D.J., Tait, C.D., Morris, D.E., 2002. Structural characterization of U(VI) in apatite by X-ray absorption spectroscopy. Environ. Sci. Technol. 36, 3114–3117. https://doi.org/10.1021/es015874f.

Retallack, G.J., 1988. Down-to-Earth approaches to vertebrate paleontology. Palaios 3, 335–344. https://doi.org/10.2307/3514662.

Schoeninger, M.J., Hallin, K., Reeser, H., Valley, J.W., Fournelle, J., 2003. Isotopic alteration of mammalian tooth enamel. Int. J. Osteoarchaeol. 13, 11–19. https://doi.org/10.1002/oa.653.

Trauth, M.H., Maslin, M.A., Deino, A., Strecker, M.R., 2005. Late Cenozoic moisture history of east Africa. Science 309, 2051–2053. https://doi.org/10.1126/science.1112964.

Trueman, C.N., 2013. Chemical taphonomy of biomineralized tissues. Palaeontology 56, 475–486. https://doi.org/10.1111/pala.12041.

Trueman, C.N., Behrensmeyer, A.K., Potts, R., Tuross, N., 2006. High-resolution records of location and stratigraphic provenance from the rare earth element composition of fossil bones. Geochem. Cosmochim. Acta 70, 4343–4355. https://doi.org/10.1016/j.gca.2006.06.1556.

Trueman, C.N., Tuross, N., 2002. Trace elements in recent and fossil bone apatite. In: Kohn, M.J., Rakovan, J., Hughes, J.M. (Eds.), Phosphates: Geochemical, Geobiological and Materials Importance, Reviews in Mineralogy & Geochemistry. Mineralogical Society of America, Washington, D.C., pp. 489–522. https://doi.org/10.1515/9781501509636-016

Turner-Walker, G., 2008. The chemical and microbial degradation of bones and teeth. In: Pinhasi, R., Mays, S. (Eds.), Advances in Human Palaeopathology. John Wiley & Sons, Ltd, Chichester, UK, pp. 3–29.

Tütken, T., Vennemann, T.W., Pfretzschner, H.-U., 2008. Early diagenesis of bone and tooth apatite in fluvial and marine settings: constraints from combined oxygen

isotope, nitrogen and REE analysis. Palaeogeogr. Palaeoclimatol. Palaeoecol. Beyond documenting diagenesis: The fifth international bone diagenesis workshop 266, 254–268. https://doi.org/10.1016/j.palaeo.2008.03.037.

Van Bocxlaer, B., Damme, D.V., Feibel, C.S., 2008. Gradual versus punctuated equilibrium evolution in the Turkana Basin molluscs: evolutionary events or biological invasions? Evolution 62, 511–520. https://doi.org/10.1111/j.1558-5646.2007.00296.x.

Wang, Y., Cerling, T.E., 1994. A model of fossil tooth and bone diagenesis: implications for paleodiet reconstruction from stable isotopes. Palaeogeogr. Palaeoclimatol. Palaeoecol. Stable Isotope and Trace-Element Geochemistry of Vertebrate Fossils: Interpreting Ancient Diets and Climates 107, 281–289. https://doi.org/10.1016/0031-0182(94)90100-7.

Xia, K., Weesner, F., Bleam, W.F., Helmke, P.A., Bloom, P.R., Skyllberg, U.L., 1998. XANES studies of oxidation states of sulfur in aquatic and soil humic substances. Soil Sci. Soc. Am. J. 62, 1240–1246. https://doi.org/10.2136/sssaj1998.03615995006200050014x.

Yaalon, D.H., Kalmar, D., 1978. Dynamics of cracking and swelling clay soils: displacement of skeletal grains, optimum depth of slickensides, and rate of intra-pedonic turbation. Earth Surf. Process. 3, 31–42. https://doi.org/10.1002/esp.3290030104.